Journal of Hydrology 609 (2022) 127657

Contents lists available at ScienceDirect

Journal of Hydrology

journal homepage: www.elsevier.com/locate/jhydrol

Research papers

Dynamic coevolution of baseflow and multiscale groundwater flow system during prolonged droughts

Chao Wang [a,b,c,*], Jesus D. Gomez-Velez [b,c,d], John L. Wilson [a]

[a] Hydrology Program, Department of Earth and Environmental Science, New Mexico Institute of Mining and Technology, Socorro, NM 87801, USA
[b] Department of Civil and Environmental Engineering, Vanderbilt University, Nashville, TN 37235, USA
[c] Consortium for Risk Estimation with Stakeholder Participation (CRESP), Vanderbilt University, Nashville, TN 37235, USA
[d] Department of Earth and Environmental Science, Vanderbilt University, Nashville, TN 37235, USA

ARTICLE INFO

This manuscript was handled by Jiri Simunek, Editor-in-Chief, with the assistance of Hoori Ajami, Associate Editor

Keywords:
Baseflow
Groundwater flow system
Deep groundwater
Mountainous watersheds

ABSTRACT

Field and numerical studies suggest that baseflow is composed of waters from a spectrum of groundwater flow paths termed the Groundwater Flow System (GWFS) – from shallow hillslope contributions to watershed-scale deep circulation originating in headwaters and discharging into lowland rivers. Here, we explore the evolution of the GWFS under prolonged droughts to understand its dynamics and multiscale nature, and to elucidate its role in baseflow generation and recession at the watershed scale. We consider three drought scenarios of varying severity and simulate groundwater flow in a 2-D cross-section of an idealized watershed with deep permeable bedrock, tracking the evolution of flow paths, baseflow, and residence times during the recession process. We find that baseflow generation at different drainage stages, and within different subwatersheds, is influenced distinctly by flow paths of different scales, depending on the relative strength of the flow paths and the position of the subwatersheds relative to the recharge/discharge zones of the deeper watershed-scale groundwater circulation. Despite having the same local relief, geology, and climate, baseflow from each subwatershed has a distinct recession behavior and time-dependent residence time distribution. Also, the hydraulic and transport characteristics of baseflow generation co-evolve and are strongly affected by the connection state of the water table to subwatersheds. These findings suggest that asynchrony and dissimilarity of baseflow generation from hillslopes under the impact of the watershed-scale groundwater flow, and interactions with local-scale and intermediate-scale groundwater flow, must be taken into account when interpreting baseflow recession data and building conceptual baseflow models at the watershed scale.

1. Introduction

Baseflow, supplied by groundwater discharge to surface water bodies, is a critical streamflow component and acts as a nexus connecting subsurface and surface hydrological, geochemical, and ecological environments (Beck et al., 2013; Fan et al., 2013; Yao et al., 2017; Berghuijs et al., 2016; Jasechko et al., 2016; Trancoso et al., 2017; Sabo et al., 2016; Maher and Chamberlain, 2014). For example, baseflow contributes to more than 50% of mean annual streamflow in more than 50% of global land area (Beck et al., 2013), and serves as the primary source of stream water in arid/semiarid regions and during dry seasons or long-term droughts (Brutsaert, 2008; Stoelzle et al., 2014; Barnhart et al., 2016; Miller et al., 2016). As inferred from streamflow temperature measurements, baseflow is composed of a water from a spectrum of flow paths with significant contributions from deep groundwater at half of U.S. stream measurement sites with natural baseflow (Hare et al., 2021). From chemical and biogeochemical perspectives, during the baseflow generation process the spatial and temporal distribution of recharge and solute sources (e.g., weathering products and nutrients), and their mixing with the groundwater in storage, can influence solute transformation, accumulation, and export to surface water bodies, with implications for surface water salinization, acidification and eutrophication (Stoddard, 1994; Valett et al., 1996; Burns et al., 1998; Tomer and Burkart, 2003; Kaushal et al., 2018). Understanding the baseflow generation process is not only important for hydrological purposes such as streamflow prediction and drought mitigation, but it is also important for understanding and simulating geophysical, geochemical, ecological, and environmental processes in which the baseflow generation process

* Corresponding author.
E-mail address: chao.wang.1@vanderbilt.edu (C. Wang).

https://doi.org/10.1016/j.jhydrol.2022.127657
Received 17 June 2021; Received in revised form 31 January 2022; Accepted 21 February 2022
Available online 2 March 2022

is actively involved.

Baseflow generation is often conceptualized as discharge from groundwater stored in an unconfined aquifer resting on a horizontal or inclined impermeable bedrock (see e.g., Troch et al., 2013 for a review). This hillslope-centric conceptualization is commonly modelled by the Boussinesq equation or its variants (most often in cross section; see e.g., Rupp and Selker, 2006 for a review), and is widely used to understand baseflow recession and its controlling factors, estimate watershed geomorphic and hydrogeologic parameters, and conceptualize watershed rainfall-runoff processes. This hillslope-centric conceptualization greatly simplifies real world landscape conditions, such as complex topography and geology (Zecharias and Brutsaert, 1988; Tague and Grant, 2004; McGuire et al., 2005; Gleeson and Manning, 2008; Yao et al., 2017; Rapp et al., 2020; Condon et al., 2020), and it cannot represent hydrological processes occurring at multiple spatial scales beyond that of hillslopes. It cannot be used to explain watershed-scale emergent baseflow generation behavior with active contribution from deep bedrock groundwater exfiltration, such as the spatial scaling of baseflow proportion and solute concentration (Frisbee et al., 2011; Frisbee et al., 2017; Asano et al., 2020; Iwasaki et al., 2021) and the connection between dynamically active drainage density and baseflow recession characteristics at the watershed scale (Biswal and Marani, 2010; Mutzner et al., 2013; Ghosh et al., 2016; Prancevic and Kirchner, 2019).

Baseflow can be sustained by a groundwater flow system (GWFS) characterized by flow paths of different scales, such as those within riparian zones and hillslopes, and watershed-scale deep groundwater flow paths connecting headwaters and main streams (Winter et al., 1998; Jiang et al., 2014; Rumsey et al., 2015). Baseflow generation from riparian zones or hillslopes can be more important in rainstorm event-scale streamflow generation and flood forecasting, or when estimating hillslope and small catchment-scale geomorphic and hydrogeologic properties. Baseflow generation from the larger, watershed-scale flow paths of the GWFS can be more important in hydrogeochemical, hydrogeomorphic, and hydrogeophysical processes that have longer characteristic time scales than typical rainstorm-flood events, such as sustaining ecological flow during prolonged droughts, post-remediation contaminant export, higher-order stream erosion and sediment transport, and long-term watershed solute budgets (Tóth, 2009; Smerdon et al., 2012; Gomez and Wilson, 2013; Miller et al., 2016; Huang and Niemann, 2006; Zhang et al., 2018). The origin of baseflow is often inferred from environmental-tracer-aided end-member separation and travel-time analysis (e.g., Ameli et al., 2018; Asano and Uchida, 2012; Frisbee et al., 2011; Lyon et al., 2015; Rademacher et al., 2005). The relative importance of baseflow originating from flow paths of different scales within the GWFS is controlled by watershed climate, vegetation, geology and geomorphological conditions (Dierauer et al., 2018; Goderniaux et al., 2013; Lovill et al., 2018; Rumsey et al., 2015; Miller et al., 2016). The role of the multiscale GWFS, especially inter-subwatershed subsurface flow paths, in watershed hydrology is gaining increasing attention from the research community and has been shown to influence watershed-scale streamflow generation and solute transport, land surface processes, and climate modeling (Ameli et al., 2018; Fan et al., 2019; Frisbee et al., 2011; Frisbee et al., 2017; Krakauer et al., 2014; Peralta-Tapia et al., 2015).

Despite some distinct and interesting features of potential contribution of multiple-scale GWFS to baseflow generation revealed by a few field studies (e.g., Ameli et al., 2018; Frisbee et al., 2011; Peralta-Tapia et al., 2015), we lack a comprehensive understanding on how baseflow and flow paths of multiple scales in the GWFS evolve during the dry season or under a long-term drought. This lack of understanding is partly due to the scarcity of distributed observations on subsurface hydrological processes and the traditional disregard of the deep flow paths of the GWFS in watershed hydrology studies. Because of this lack of understanding, the role of the dynamics of the multiscale GWFS is seldom considered in baseflow hydrograph analysis and in parameterizing baseflow component in conceptual hydrological models (e.g., Clark et al., 2016; Fan et al., 2019; Piovano et al., 2020). In order to improve the conceptualization and parsimonious modeling of baseflow generation in watersheds influenced by multiscale GWFSs, it's important to clarify the distinct roles of the different-scale flow components of the GWFS in baseflow generation.

In this study, we analyze baseflow generation, and the coevolution and roles of flow paths of different scales in the GWFS, under prescribed long-term droughts in a 2-D vertical cross section of an idealized high order watershed (Fig. 1a). The cross section of the idealized watershed is characterized by a sinusoidal topography with a linear regional slope and a homogeneous deep permeable bedrock which simplifies the bedrock permeability depth profile and the shallow highly permeable soil and weathered bedrock zone that could exist in some, but not all, natural watersheds. This simple conceptualization dramatically extends the hillslope model to include deep groundwater. We hypothesize that baseflow generation and recession behaviour are significantly and distinctly affected by the dynamics and interactions of flow paths at scales larger than that of typical riparian zones and hillslopes. We test our hypothesis by exploring the time-varying dynamics of both baseflow generation and the multiscale GWFS, and the relationships between them. Specifically, we focus on the relationship between baseflow discharge and groundwater storage, and the relationship between baseflow residence time and groundwater age, which are the two fundamental constitutive relationships widely used in parsimonious lumped watershed streamflow generation and solute transport modeling, respectively. Our simple 2D conceptualization, which preserves the ideas of neighboring subwatersheds, allows us to address the essence of our research questions without the additional complexity of a stream network. We show that, even with simple topographic and hydrogeologic settings, complex and scale-dependent baseflow dynamics emerge due to the changing effects of the multiscale GWFS on baseflow generation in different subwatersheds and during the different stages of prolonged droughts. This study provides mechanistic and conceptual understanding of watershed-scale baseflow generation from the multiscale GWFS. The additional complexity introduced by the stream network pattern can be addressed in future studies; it is not expected to change the crux of our new findings.

2. Methods

2.1. Prescribed Long-term Droughts as Simple Forcings

To reveal the effects of prolonged droughts, we start with a fully-saturated steady-state GWFS, where the water table coincides with the topography (e.g., a wet climate and/or low conductivity permeable media), and compute the amount and spatial distribution of recharge along the top boundary. The initial flow system can be created by applying a relatively large spatially-uniform recharge to raise the water table to the land surface over the entire model domain. To represent a drought we change the boundary to one with a prescribed, uniform potential recharge rate (we ignore the effect of topography or vegetation on recharge) that is lower than the average recharge rate for the fully-saturated case. We use a spatially-constant recharge rate of zero to represent a hypothetical extreme drought. We also use two nonzero reduced uniform potential recharge rates to represent droughts of less severity; these rates are equal to one twentieth (14.8 mm/yr) and one half (148.0 mm/yr) of the spatially-averaged recharge rate found for the pre-drought fully-saturated case (295.5 mm/yr). The 295.5 mm/yr recharge rate for the pre-drought fully-saturated case is reasonable and exists in natural bedrock watersheds (e.g., the Santa Ynez Mountains of Southern California). The two nonzero reduced recharge rates (14.8 mm/yr and 148.0 mm/yr) represent moderate and mild droughts, respectively. The three droughts with 0, 14.8 mm/yr and 148.0 mm/yr recharge rates allow the system to reach three different representative final equilibrium states (Section 3). Note that, at fully-saturated

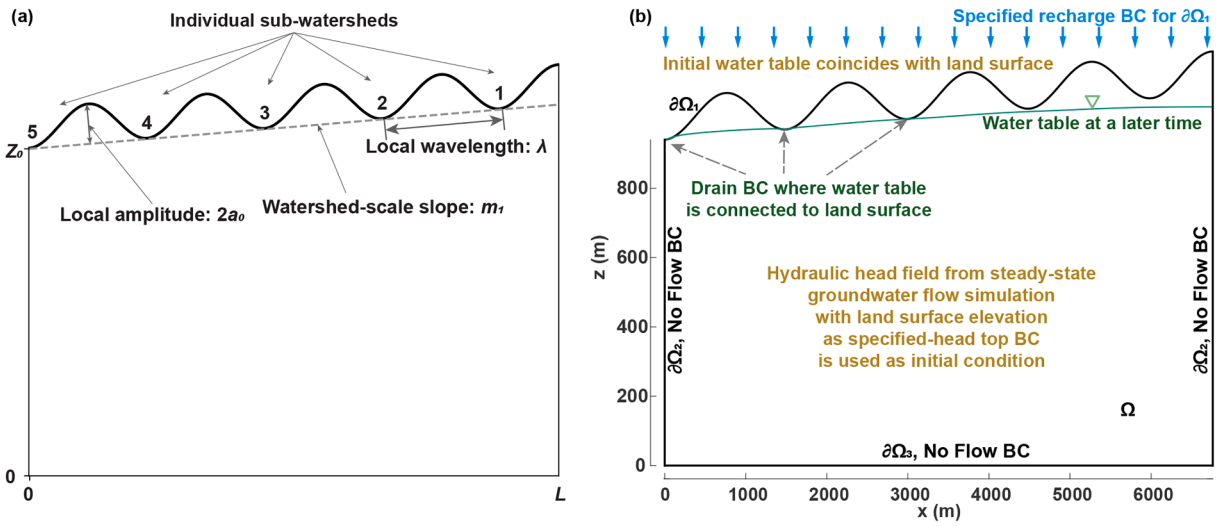

Fig. 1. (a) Model domain (not to scale) and topography parameters. (b) Initial and boundary conditions for groundwater flow and baseflow generation model.

locations where the water table coincides with the land surface, part or all applied potential recharge is rejected by the system, creating a spatially non-uniform distribution of net recharge accepted by the system for the initial flow field and the flow field during drainage under the moderate and mild drought scenarios.

This type of simple forcing is used for three reasons. (1) This system configuration is representative of real situations when a watershed in a humid region experiences a prolonged drought (Haitjema and Mitchell-Bruker, 2005; Gleeson and Manning, 2008; Condon and Maxwell, 2015). (2) Different stages of the long-term drainage represent average drainage conditions of watersheds in different climate regions (Dai et al., 2021). (3) The emphasis of this study is on the role of the dynamical GWFS in baseflow generation at multiple spatial scales and the control of topographic structure. Even though using more complex recharge forcing with spatial–temporal variations in intensity, duration and intermittency can add an additional level of complexity to stimulate new insights into the system response, it can also obscure the role of topography and the dynamical GWFS in baseflow generation. System response under more complex recharge conditions with the interactive effect of topographic structure bears its own importance and can be explored in a separate study.

2.2. Model Domain Configuration

Groundwater flow and transport modeling in cross-sectional domains has been, and is, widely used to study fluxes and age distributions in GWFSs. In particular, 2-D simplified representations are parsimonious tools that allow us to gain insights into the role of key topographic and geologic features on the flow and transport characteristics in GWFSs (e.g., Tóth, 1963; Freeze and Witherspoon, 1966; Tóth, 2009; Cardenas and Jiang, 2010; Gomez and Wilson, 2013; Welch and Allen, 2014; Gleeson et al., 2016). In this study, groundwater flow and transport are simulated in a 2-D vertical cross section of an idealized watershed to investigate the dynamics of baseflow and a GWFS during prolonged droughts. The topography of the top boundary and land surface of the 2-D cross section is represented by

$$z_s(x) = z_0 + a_0 + m_1 x + a_0 \sin\left(\frac{2\pi}{\lambda}x + \frac{3\pi}{2}\right) \quad (1)$$

where z_0 determines the depth [L] of the basin below the lowest point of land surface, m_1 represents the watershed-scale topographic slope [-], and a_0 and λ represent the amplitude [L] and wavelength [L] of the sinusoidal local relief, respectively. The parameter values used in this study are $z_0 = 1000$ m, $m_1 = 0.02$, $a_0 = 60$ m, $\lambda = 1500$ m, and $x \in [0, L_x]$ with $L_x = 6760$ m (we also varied most of these geometric parameters in sensitivity analyses which, for brevity, we haven't included here; they don't change the core of our findings). This 2-D domain can be viewed as a transverse cross section of a 3-D watershed (see, e.g., Fig. 1 in Cardenas, 2007 for an illustration). The regions between neighbouring peaks are designated as subwatersheds and are numbered 1–5 from high elevation upstream to low elevation downstream (Fig. 1a). For our 2-D domain, the ratio of the linear regional topographic rise to the local topographic amplitude is $m_1 L_x / a_0 = 2.25$ and the ratio of the width of the domain to the local topographic wavelength is $L_x/\lambda = 4.5$. These dimensionless ratios measure the topographic structure and relative strengths of the local- and the regional-scale groundwater flow paths, and can be used in future studies on the control of topographic structure on baseflow generation.

The 2D Tothian conceptualization has played an unprecedented role in improving our understanding of multiscale GWFSs (Anderson, 2008), but to the best of our knowledge, it has never been used to study the dynamics of watershed-scale baseflow generation (e.g., discharge sensitivity and transient residence time distribution) and its relationship to multiscale GWFSs as we do in this paper. Nor have more complex 3D conceptualizations, ones that recognize deep groundwater, attempted to address this topic.

2.3. Groundwater Flow and Baseflow Simulation

We use the finite difference code MODFLOW-NWT (Niswonger et al., 2011; Harbaugh, 2005) to simulate saturated groundwater flow (Eq. 2, below) in the 2D model domain (Fig. 1b), while accounting for gravity drainage from the vadose zone through the phreatic-surface boundary condition (Eq. 5, below) (Bear, 1972). The spatiotemporal variation of the phreatic surface (i.e., the water table) is unknown, and is estimated as part of the numerical non-linear solution. Vadose-zone capillary effects are negligible in this drainage situation as the vertical scale of the 2D saturated flow (10s to 100s of meters) is much larger than the length scale of capillary forces (Dagan and Kroszynski, 1973; Dagan, 1989), e.g., Gardner's capillary-length parameter (which ranges from ~0.1 to 5 m in typical permeable geological media). This is why, for example, groundwater well tests in phreatic aquifers almost always ignore the effects of capillary forces on delayed yield (Tartakovsky and Neuman, 2007). We also neglect compressibility effects, as the phreatic surface drops much too slowly over time for compressibility to have any effect. Storage depletion is entirely due to draining the porous media specific yield at the phreatic surface (Eq. 5, below). We assume that the effective porosity for groundwater flow and the specific yield are equal to the

porous media porosity.

We track the evolution and location of the hydraulic head at the top layer to define fluxes across the land surface. Specifically, if the hydraulic head at the top layer is higher than or equal to the land surface elevation, we use a drain boundary condition to simulate head-dependent drainage flux (Eq. 4), which becomes stream baseflow and is removed from the model. This is also a seepage face boundary condition. The drain elevation is set to be land-surface elevation. The drain flux (baseflow) is calculated as the drain conductance C_D times the difference between top layer hydraulic head and the drain elevation (Eq. 4). On the other hand, if the hydraulic head at the top layer is lower than the land surface, we impose a phreatic surface boundary with prescribed recharge (Eq. 5) (Bear, 1972). As the water table drops during the mild and moderate droughts, the discharge area decreases and the recharge area, and therefore the total recharge, increases. No flow boundary conditions are assumed at the lateral and bottom boundaries (Eq. 6). Under these assumptions, the mathematical statement for flow is given by

$$\nabla\cdot(\mathbf{K}\nabla h) = 0, \quad \mathbf{x}\in\Omega, t>0 \tag{2}$$

$$h(\mathbf{x}, t=0) = h_0(\mathbf{x}), \quad \mathbf{x}\in\Omega \tag{3}$$

$$\mathbf{n}\cdot(-\mathbf{K}\nabla h) = C_D(h-z_s)+\mathbf{R}\cdot\mathbf{n}, \quad h\geqslant z_s, \mathbf{x}\in\partial\Omega_{1,out}, t>0 \tag{4}$$

$$\frac{\partial h}{\partial t}+\frac{1}{\phi}(-\mathbf{K}\nabla h-\mathbf{R})\cdot\nabla(h-z) = 0, \quad h<z_s, \mathbf{x}\in\partial\Omega_{1,wtb}, t>0 \tag{5}$$

$$\mathbf{n}\cdot(\mathbf{K}\nabla h) = 0, \quad \mathbf{x}\in\partial\Omega_2\cup\partial\Omega_3, t>0 \tag{6}$$

where h is hydraulic head [L], $\mathbf{K}$ is hydraulic conductivity tensor [LT^{-1}] and is assumed to be homogeneous and isotropic in this study, t is time [T], $\mathbf{x}$ is coordinate vector [L], C_D is the drain conductance per unit surface area [T^{-1}], z_s is land surface elevation [L], $\mathbf{R} = -R\nabla z$ is recharge flux per unit area of porous media [LT^{-1}], R is the magnitude of recharge [LT^{-1}], ϕ is effective porosity with respect to flow [-] and is assumed to be constant and equal to the specific yield S_y, Ω represents the modeling domain, $\partial\Omega_{1,out}$ represents the top land surface boundary where hydraulic head is higher than or equal to the land surface elevation, $\partial\Omega_{1,wtb}$ represents the top water table boundary where water table is below the land surface, $\partial\Omega_2$ represents the lateral boundaries, $\partial\Omega_3$ represents the bottom boundary, and $\mathbf{n}$ is the outward normal vector at any point on the boundary of Ω. The property values in this study are $\mathbf{K} = K\mathbf{I}$ with $K = 0.01$ m/day and $\mathbf{I}$ the identity matrix, $C_D = 0.4$ day^{-1}, and $\phi = 0.03$. The conductivity and porosity values are typical for permeable rock systems, especially sandstones (e.g., Dingman, 2015), but to account for other possible values our results are presented dimensionlessly (see below). The drain conductance is high, indicating little "surface" resistance (e.g., a clogged streambed) to discharging groundwater. The recharge, $\mathbf{R} = -R\nabla z$, has rates $R = 14.8$ or 148.0 mm/yr for the moderate and mild drought scenarios, respectively. These rates are typical of relatively dry to somewhat more humid bedrock systems, respectively.

During the drainage, the water table is defined as the phreatic surface where the pressure head is zero (i.e., places where the hydraulic head equals elevation head or $\{\mathbf{x}|h(\mathbf{x}) = z\}$), and it is described by the nonlinear kinematic boundary condition in Eq. (5), which is based on the continuity of water flux across the phreatic surface along the normal vector (Bear, 1972; Dagan, 1989). MODFLOW-NWT treats cells above the water table as "dry cells" (water content $\theta = 0$) and cells below the water table as fully saturated ($\theta = \theta_s$), where θ_s is saturated water content and is assumed to be equal to porosity. Flux out of the model domain across the drain boundary is lumped at each time step for each subwatershed (Fig. 1a) and for the entire domain to get the baseflow discharge.

The initial condition (i.e., initial hydraulic head) for the drainage, $h_0(\mathbf{x})$, is taken as the solution of the steady-state fully-saturated groundwater flow problem (Eq. 7) with land surface elevation as a specified hydraulic head top boundary condition (Eq. 8) with no flow lateral and bottom boundary conditions (Eq. 9), as represented by the following mathematical statement

$$\nabla\cdot[\mathbf{K}\nabla h_0] = 0, \quad \mathbf{x}\in\Omega \tag{7}$$

$$h_0(x, y, z = z_s(x, y)) = z_s(x, y), \quad (x, y)\in\partial\Omega_1 \tag{8}$$

$$\mathbf{n}\cdot(\mathbf{K}\nabla h_0) = 0, \quad \mathbf{x}\in\partial\Omega_2\cup\partial\Omega_3 \tag{9}$$

where $\partial\Omega_1$ is the entire top boundary of the model domain. The recharge rate, $R(\mathbf{x})$, at the land surface needed to sustain the steady-state groundwater flow field is calculated at the constant head boundary ($\partial\Omega_1$) based on the simulated hydraulic head.

For the case of a hypothetical long-term extreme drought represented by zero recharge top boundary condition ($R = 0$, Section 2.1), the GWFS asymptotically approaches a static-state with the water table as a flat surface on the same level of the lowest drainage point of the domain (i.e., $h(\mathbf{x}) = z_s(x = 0) = z_0$, Fig. 1, Eq. 1). For the case of a less severe drought represented by a reduced non-zero recharge top boundary condition, the GWFS asymptotically approaches a steady-state with water table as a subdued imitation of the land surface. The mathematical statement for this final steady-state groundwater flow field can be derived from the mathematical statement of the transient drainage problem (Eqs. (2)–(6)) by removing the initial condition Eq. 3 from the original mathematical statement and letting $\partial h/\partial t\to 0$ in Eq. 5. Thus, the groundwater flow field during drainage under a non-zero reduced recharge approaches the solution of the following mathematical statement

$$\nabla\cdot(\mathbf{K}\nabla h) = 0, \quad \mathbf{x}\in\Omega \tag{10}$$

$$\mathbf{n}\cdot(-\mathbf{K}\nabla h) = C_D(h-z_s)+\mathbf{R}\cdot\mathbf{n}, \quad h\geqslant z_s, \mathbf{x}\in\partial\Omega_{1,out} \tag{11}$$

$$\frac{1}{\phi}(-\mathbf{K}\nabla h-\mathbf{R})\cdot\nabla(h-z) = 0, \quad h<z_s, \mathbf{x}\in\partial\Omega_{1,wtb} \tag{12}$$

$$\mathbf{n}\cdot(\mathbf{K}\nabla h) = 0, \quad \mathbf{x}\in\partial\Omega_2\cup\partial\Omega_3 \tag{13}$$

During the drainage under the extreme and moderate drought scenarios, the water table disconnects sequentially from the subwatersheds. We define a drainage stage as the drainage time period between two consecutive disconnections of water table from the land surface of subwatersheds. Critical differences of drainage behavior occur when the water table is connected to a different number of subwatersheds. Our three drought scenarios are essentially designed to have different numbers of subwatersheds attached to the water table as the system approaches a final steady state. Our extreme, moderate, and mild drought scenarios lead to water table disconnection from all, two, and no subwatersheds, respectively, as the system approaches final steady state (Section 3.1.1).

2.4. Spatial and Temporal Discretization

The domain (Fig. 1a) is discretized into cuboid cells with dimensions in the horizontal (i.e., x and y) directions $\Delta x = \Delta y = 10$ m. This results in 676 columns of cells in the x-direction and one row of cells in the y-direction. The vertical (i.e., z) direction is discretized into 500 layers, which are indexed by integers $k = 0$ to 499 from the top to the bottom. The thickness of the first layer ($k = 0$) is set to be 0.5 m uniformly over the entire domain. The rest of the layers are grouped into shallow (layers $k = 1$ to 200), intermediate (layers $k = 201$ to 300) and deep (layers $k = 301$ to 499) zones. For each location (x, y), layer thickness is constant within each of the shallow, intermediate and deep zones, and the ratio of layer thicknesses of the three zones is 1:2:4. Because the total thickness of the domain varies at different (x, y) locations, the layer thickness

within each zone also varies at different (x,y) locations. The layer thicknesses within the three zones are in the ranges $[0.84, 1.05]$ m, $[1.67, 2.10]$ m and $[3.34, 4.20]$ m.

We drain the domain for 1 million days (2,738 years) to study the baseflow generation behavior during the full range of watershed storage condition from fully-saturated to nearly zero drainable storage for the case of an extreme drought with zero recharge. At the end of the simulation, the drainable storage reaches 0.04% the initial drainable storage. For the case of a reduced non-zero recharge, running the model 1 million days ensures the final flow field to be very close to the steady-state flow field described by Eqs. (10)–(13). A total of 1,000 time steps are used and the time step duration changes according to a geometric progression (Harbaugh, 2005). A time step multiplier, which is the ratio of the duration of each time step to that of the preceding time step, equal to 1.011 is used. The size of the time steps ranges from 0.19 day at the beginning of the drainage process to 10,880 days at the end of the simulation.

2.5. Estimation of Groundwater Age and Residence Time Distributions

Groundwater age is the time it takes for a particular water parcel to flow from the water table at its recharge location to the location within the aquifer where it is sampled physically or studied theoretically (Kazemi et al., 2006). Groundwater residence time is the time it takes for a water parcel to travel from the recharge area to the discharge area (e.g., streams, springs, wells). Groundwater discharge into streams provides stream baseflow. Baseflow residence time (typically called travel or transit time by the surface water hydrology community; they often use the term residence time to represent something similar to the groundwater community's "age") is defined as the time for a water parcel to travel from its entrance into the watershed as recharge to its discharge into the streams as baseflow. So, by definition, groundwater residence time equals baseflow residence time.

Groundwater age of a water parcel in storage is calculated using forward particle tracking. The particle tracking is started for the fully-saturated steady-state groundwater flow (Eqs. (7)–(9)) 3×10^6 days (8,214 years) before the beginning of the drainage (i.e., a spin-up phase to fill up the domain with particles) and run afterwards for 1×10^6 days (2,738 years) in the transient flow field induced by the drainage (Eqs. (2)–(6)). A tracking time duration of 3×10^6 days in the initial fully-saturated steady-state groundwater flow is close to the longest residence time of the steady-state flow field that can be identified with the largest spatial density of particles that our computational capacity can support (Support Information Text S1 and Fig. S1).

In the forward tracking, particles are released during the progression of the simulation and each particle is used to represent a volume of about $V_{p,0} = 2\ \mathrm{m}^3$ recharge (assuming a 10 m width for the cross section in the y direction). This is equivalent to about 1.2 million particles to fill the model domain. The choice of $V_{p,0} = 2\ \mathrm{m}^3$ is a trade-off between computational capacity and achieving smooth enough baseflow residence time distributions (RTDs). The actual recharge volume represented by each particle is adjusted to ensure that an integer number of particles are released during each MODFLOW time step. Text S2 presents the details of the particle releasing strategy. A total number of 82,004,388 and 92,084,407 particles are used for the simulations under the extreme and mild drought scenarios, respectively.

Particle tracking is performed using MODPATH Version 6 (Pollock, 2012). MODPATH tracks numerical particles in the groundwater flow field using a semi-analytical tracking algorithm. Particle velocities across cell faces are calculated using Darcy's law based on hydraulic heads from the solution to the groundwater flow problem (Section 2.3) and an effective porosity $\phi = 0.03$. A bilinear interpolation is used to calculate particle velocity within each cell and analytical formulas are derived for the particle travel time and exit location in each cell. Only advective transport is simulated by the particle tracking and dispersion and reaction are ignored. The readers are referred to (Pollock, 2012) for more details about the algorithm. The pre- and post-processing for MODFLOW and MODPATH modeling are assisted by the Python package FloPy (Bakker et al., 2016).

The groundwater-age distribution and groundwater residence time distribution (RTD) are calculated for any time of interest as the probability distribution of groundwater age and groundwater residence time associated with particles, with the probability of particle age proportional to the volume of recharge represented by the particle. Then we can get

$$S^{pt}(\tau < T, t) = \sum_{pid \in \Omega^{pt}_{S(\tau<T,t)}} V^{pid} \tag{14}$$

$$S^{pt}(t) = \sum_{pid \in \Omega^{pt}_{S(t)}} V^{pid} \tag{15}$$

and

$$Q^{pt}(\tau < T, t) = \sum_{pid \in \partial\Omega^{pt}_{Q(\tau<T,t)}} V^{pid} \tag{16}$$

$$Q^{pt}(t) = \sum_{pid \in \partial\Omega^{pt}_{Q(t)}} V^{pid} \tag{17}$$

where V^{pid} is the water volume associated with the particle numbered pid, $S^{pt}(\tau < T, t)$ is the total volume $[\mathrm{L}^3]$ of water parcels associated with particles in storage with age less than T at time t, $S^{pt}(t)$ is the total volume $[\mathrm{L}^3]$ of water parcels associated with all particles in storage at time t, $Q^{pt}(\tau < T, t)$ is the total volume of water parcels associated with particles with residence time less than T and exiting some discharge region of interest per unit time $[\mathrm{L}^3\ \mathrm{T}^{-1}]$ at time t, $Q^{pt}(t)$ is the total volume of water parcels associated with all particles exiting the discharge region of interest per unit time $[\mathrm{L}^3\ \mathrm{T}^{-1}]$ at time t, $\Omega^{pt}_{S(\tau<T,t)}$ is the index set of particles in storage and with age less than T at time t, $\Omega^{pt}_{S(t)}$ is the index set of all particles in storage at time t, $\partial\Omega^{pt}_{Q(\tau<T,t)}$ is the index set of particles with residence time less than T and exiting some discharge region of interest in $\partial\Omega_{1,out}$, $\partial\Omega^{pt}_{Q(t)}$ is the index set of all particles exiting the discharge region of interest in $\partial\Omega_{1,out}$. Then the groundwater-age distribution and groundwater RTD in the form of cumulative distribution function at any time t can be estimated as:

$$P_S(T,t) = \frac{S^{pt}(\tau < T, t)}{S^{pt}(t)} \tag{18}$$

$$P_Q(T,t) = \frac{Q^{pt}(\tau < T, t)}{Q^{pt}(t)} \tag{19}$$

Theoretically, Eqs. (16), (17) and (19) can be used to calculate baseflow RTD at any time instant t. Practically, due to the discrete nature of the solution technique and the limit on the number of particles set by the computational capacity, the number of particles exiting the domain at any time instant t can be small and the calculated baseflow RTD can be coarse. So the baseflow RTDs presented later in Figs. 5–7 are calculated in time intervals selected using the strategy documented in Text S3.

2.6. StorAge Selection Function

StorAge Selection (SAS) function relates the age distribution of storage within and the RTD of flux out of a watershed. It's used as a closure relationship in lumped watershed-scale modeling of conservative solute transport and can be interpreted in terms of a watershed's preference for discharging water of different ages. Three slightly different but closely related formulations of SAS function exist in the literature (Botter et al., 2011; van der Velde et al., 2012; Harman, 2015).

In this paper, we use the concept of absolute StorAge Selection (aSAS) function (Botter et al., 2011) in our description of the solute retention, mixing, and releasing behavior of the multiscale GWFS. In the context of our paper, the aSAS function at any time t can be calculated as the quotient between the probability density functions of the residence time of baseflow and the age of groundwater in storage

$$\omega_Q(T,t) = \frac{p_Q(T,t)}{p_S(T,t)} = \frac{dP_Q(T,t)/dT}{dP_S(T,t)/dT} \tag{20}$$

where $p_Q(T,t)$ and $p_S(T,t)$ are the probability density functions of baseflow residence time and groundwater age, respectively.

2.7. Flushing Intensity

Flushing intensity (Zlotnik et al., 2011; Gomez-Velez et al., 2014) is an integrated measure of the capacity of the groundwater flow field to transport water mass by advection at different depths and is defined by:

$$F(z) = \frac{1}{S}\int_S \sqrt{(q_x^2(\mathbf{x}) + q_y^2(\mathbf{x}) + q_z^2(\mathbf{x}))}\, ds \tag{21}$$

where z is depth below land surface [L], q_x, q_y, q_z are components of the Darcy flux [L/T], S is the area of the layer over which the magnitude of flux is integrated [L^2]. Flushing intensity provides a quantitative measure of the groundwater flow field strength at different depths. We compare flushing intensity at different time instants of the drainage to indicate the change of the relative strength of the groundwater flow cells of different scales at different depths (Fig. S4).

2.8. Discharge Sensitivity Analysis

Assuming no water flow across the lateral boundaries of a watershed, water balance of the watershed can be described as

$$\frac{dS}{dt} = P - ET - Q \tag{22}$$

where S is storage [L^3], t is time [T], P is precipitation [L^3/T], ET is evapotranspiration [L^3/T] and Q is discharge [L^3/T] from the watershed outlet. The discharge sensitivity

$$g(Q) = \frac{dQ}{dS} \tag{23}$$

is a lumped measure of the relationship between S within and Q out of a watershed, which are two fundamental and interactively related components of water balance of a watershed. $g(Q)$ is controlled by watershed landscape conditions such as topography and hydrogeology (e.g., Brutsaert and Nieber, 1977; Zecharias and Brutsaert, 1988; Zecharias and Brutsaert, 1988; Biswal and Marani, 2010; Mutzner et al., 2013; Berghuijs et al., 2016). It is a characteristic function of watersheds and can serve as a closure relationship to solve a watershed-scale water balance equation for lumped rainfall-runoff modeling (e.g., Kirchner, 2009). A conceptual explanation of discharge sensitivity can be found in Text S4 for readers who are not familiar with this concept.

While calculating $g(Q)$ (Eq. 22) from model output at discrete time steps, the change of discharge and storage between two consecutive time steps can be approximated as $dQ = Q_{t+\Delta t} - Q_t$ and $dS = S_{t+\Delta t} - S_t$, respectively.

Since the 2-D cross sectional domain Ω used in this study (Fig. 1a) can be viewed as half of a transverse cross section of a 3-D basin (Fig. 1, Cardenas, 2007), then subwatershed 5 only captures half of the groundwater flow draining into the main stream. For this reason, the discharge from subwatershed 5, Q_5, and the drainable storage of the model domain, S, are both doubled before discharge sensitivity analysis. So the discharge sensitivity for subwatersheds and the entire domain, as a function of twice the total discharge from the entire domain Ω, are calculated in this study as:

$$g_i(Q_T) = \frac{dQ_i}{d(2S)} = \frac{1}{2}\frac{dQ_i}{dS}, \quad i = 1,2,3,4 \tag{24}$$

$$g_5(Q_T) = \frac{d(2Q_5)}{d(2S)} = \frac{dQ_5}{dS} \tag{25}$$

$$g(Q_T) = \frac{d(2\sum_{i=1}^{5} Q_i)}{d(2S)} = \frac{\sum_{i=1}^{5} dQ_i}{dS} \tag{26}$$

where $Q_i (i = 1,2,3,4,5)$ represent baseflow discharge from different subwatershed areas shown in Fig. 1a, $Q_T = 2\sum_{i=1}^{5} Q_i$ denotes twice the discharge from the entire model domain Ω, S denotes the drainable storage within Ω (Fig. 1a).

2.9. Nondimensionalization and Scaling

The dimensionless results presented in Section 3 are obtained by dividing variables by their corresponding characteristic values. The total discharge $Q_0 = 54.7$ m^3/day and the total drainable storage $S_0 = 2.6 \times 10^5 m^3$ (i.e., the total pore volume in the domain above the lowest drainage point) for the entire domain Ω of the fully-saturated steady-state model (Eqs. (7)–(9)) are used to calculate the characteristic values for discharge (Q_c), storage (S_c) and time (t_c). Following the consideration of domain symmetry in the last paragraph of Section 2.8, we use $Q_c = 2Q_0$ and $S_c = 2S_0$. The fully-saturated steady-state turnover time of the total drainable storage S_0/Q_0 is used as the characteristic time scale t_c (= 4,782 days). This time scale is used to non-dimensionalize drainage time, baseflow residence time, and groundwater age. The dimensionless discharge, storage and time are then calculated as $Q^* = Q/Q_c, S^* = S/S_c$ and $t^* = t/t_c$, respectively. Dimensionless discharge sensitivity is calculated as $g_i^*(Q_T^*) = dQ_i^*/d(2S^*) = d(Q_i/Q_c)/d(2S/S_c) = t_c \cdot (dQ_i/d(2S)) = t_c g_i(Q_T)$, for $i = 1,2,3,4$ and $g_5^*(Q_T^*) = d(2Q_5^*)/d(2S^*) = d(2Q_5/Q_c)/d(2S/S_c) = t_c \cdot (dQ_5/dS) = t_c g_5(Q_T)$. We choose the wavelength (λ) and half the amplitude ($a_0/2$) of the local topographic relief as characteristic values for the length scale and hydraulic head, respectively. The value of hydraulic conductivity (K) is selected to be the characteristic value for specific discharge (Darcy velocity). $K\lambda$ is used as the characteristic value for the stream function.

The dimensionless results presented below apply to other property values and recharge rates, in addition to those given above. To do so, the spatial geometry must remain the same. The values of K, R, C_D and ϕ can change, but they must change together so that their relative ratios remain the same.

3. Results and Discussion

3.1. Baseflow from Multiscale Groundwater Flow System

In this subsection, we analyze the baseflow recession (characterized by discharge and discharge sensitivity) and the evolution of the groundwater flow field, including the changing shape and position of the water table and the reorganization of the GWFS (characterized by hydraulic head and streamlines), for the three drought scenarios. We show that the changes in the baseflow recession behavior is closely related to the evolution of the GWFS, and that the flow paths of different scales play different roles in baseflow generation.

3.1.1. Evolution of Multiscale Groundwater Flow System

The evolution of the GWFS is characterized by the changing shape of the water table, the disconnections of the water table from subwatersheds (i.e., when the water table beneath a subwatershed completely drops below the land surface), and the reorganization of the flow field. An animation of the drainage process is provided in the

Supporting Information (Movie S1), illustrating the sequential disconnection of the water table from subwatersheds 1 to 4 under the extreme drought scenario.

At the beginning of the drainage, the water table closely follows the topography and has local- and watershed-scale relief mimicing that of the land surface topography (Fig. 2a). The GWFS can be subdivided into different flow cells. First, the local-scale flow cells are delineated by streamlines connecting hills and neighbouring valleys. Second, the intermediate-scale flow cells are delineated by streamlines connecting upstream hills and downstream valleys. Third, the watershed-scale flow cell carries flow from the highest hill to the mainstream.

As the drainage progresses, the water table drops and flattens, and the penetration depth of the local-scale flow cells decreases (Figs. 2, S2 and S3, respectively, for the extreme, moderate and mild droughts; note that, to make it easier to read the paper, when Figs. S2 and S3 are cross-referenced in company with Fig. 2, it's not mandatory for the readers to look at Figs. S2 and S3; in these cases, Fig. 2 is sufficient to support our discussion, with Figs. S2 and S3 providing additional examples and evidence.). The flushing intensity of the shallow groundwater flow field decreases faster than does the deeper intensity (Fig. S4b), indicating that the flow field becomes more controlled by the deep, watershed-scale flow component, which is driven by the watershed-scale water-table slope. Also notice that the groundwater-subwatershed divides are biased towards the upstream (right) side of the hills, due to the influence of the watershed-scale water-table slope (Figs. 2, S2 and S3). The groundwater-watershed divides also migrate further to the upstream (right) side of the hills as the drainage progresses. This means that groundwater contributing to baseflow can cross surface drainage divides and the sources can evolve during a baseflow recession event. This challenges the single hillslope conceptualization widely used to study baseflow recession behavior (e.g., Troch et al., 2013). The evolution of the groundwater flow field is also characterized by the disappearance of the local flow cells and the merging of the local groundwater flow field into the deeper, watershed-scale groundwater flow field (e.g., notice the change of the local groundwater flow field near the drainage area of subwatershed 1 shown in Figs. 2c and 2d, S2c and S2d). As is discussed in the following subsections, these features of the GWFS evolution explain features in baseflow recession behavior and the evolution of its RTD.

3.1.2. Similar/ Dissimilar Baseflow Recession Behavior from Different Subwatersheds

The decreasing pattern of subwatershed discharge $Q_i^*(t^*)$ and the magnitude of discharge sensitivity $g_i^*(Q_T^*)$ $(i = 1, 2, \ldots, 5$ for subwatersheds 1–5) are very similar for different subwatersheds during drainage stage I, which takes place before subwatershed 1 dries up (Figs. 3, S5 and S6), despite differences in the rate of recharge during the drought. The similarity of $g_i^*(Q_T^*)$ is a result of the similar hydraulic response of local subwatershed-scale flow cells to the drought during this early stage of the drainage. This is revealed by the similar spatial patterns of hydraulic head contours and instantaneous streamlines near the discharge regions of subwatersheds 1–5 (Figs. 2a and 2b, S2a and S2b, S3). At any time instant, the discharge, discharge sensitivity, and the change of water-table shape, are determined by the instantaneous shape of the water table and the topography where the water table remains attached to the land surface (Eqs. (4) and (5)). The similar patterns of the local-scale flow cells can be attributed to the similar undulations of the local water table, which is a subdued imitation of the local topographic relief (Figs. 2a and 2b, S2a and S2b, S3). This indicates the dominant control of local landscape and groundwater flow field on baseflow discharge dynamics during the early stage of recession.

For drainage under the extreme drought scenario, after the disconnection of water table from subwatershed 2 at the end of drainage-stage II, the discharge sensitivity $g_i^*(Q_T^*)$ $(i = 3, 4, 5)$ for the subwatersheds start to deviate more from each other (Fig. 3d). Complex shapes for $g_4^*(Q_T^*)$ and $g_5^*(Q_T^*)$ emerge after subwatershed 3 dries up at the end of drainage-stage III. Similar evolution patterns of $g_i^*(Q_T^*)$ occur during drainage stages II and III under the moderate drought (Figs. 3e and S6). Additionally, the deviation of $g_i^*(Q_T^*)$ $(i = 1, 2, 3, 4, 5)$ from each other becomes more dramatic as the watershed-scale topographic slope, m_1, increases (not shown). In a domain with relatively gentle watershed-scale topographic slope, the local-scale flow cells during the early stage of the drainage are driven more by local water-table undulations

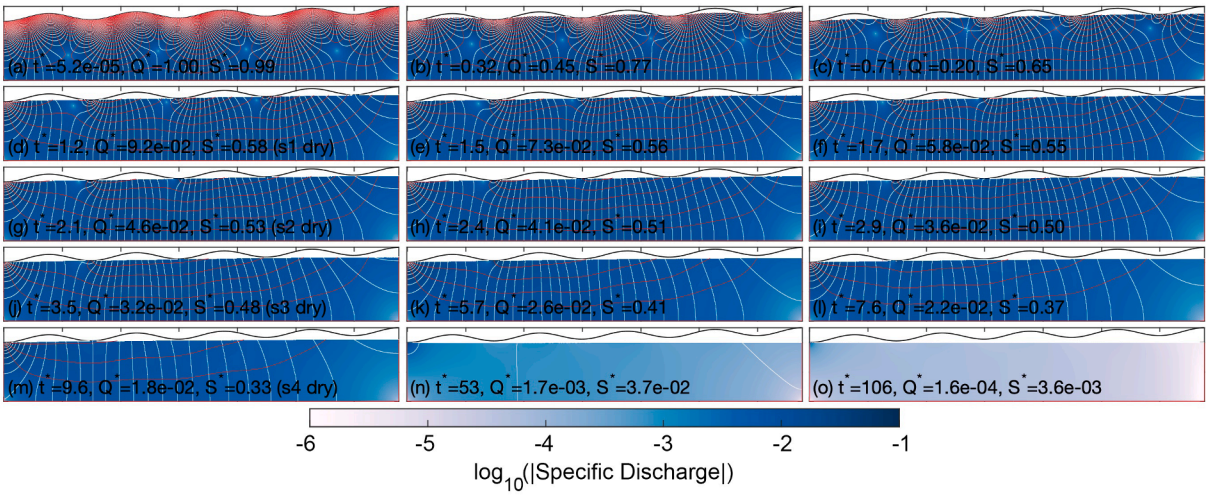

Fig. 2. Spatio-temporal evolution of the flow field during the drainage process. Instantaneous hydraulic head (white contour curves) and streamlines (red contour curves), and the magnitude of dimensionless specific discharge (color patch) are shown at selected time instants during the drainage under the extreme drought scenario. The dimensionless time t^*, discharge Q^* from and drainable storage S^* within the entire domain Ω are shown in the lower, left corner of each snapshot. Nondimensionalization method is described in Section 2.9. Time instants are selected to distribute evenly on $\log_{10}Q^*$ scale within each interval between disconnections of water table from subwatersheds. Plots (d), (g), (j) and (m) correspond to the time instants when the water table disconnects from subwatersheds 1, 2, 3 and 4, respectively, as indicated in the labels by '*si* dry' $(i = 1, 2, 3, 4)$. The area of groundwater discharge (i.e., seepage faces) near local topographic lows starts out covering almost half the domain and then decreases rapidly over time, drying up as subwatersheds are disconnected from the water table. Streamlines are created by treating the flow field at each time instant as steady-state. All panels have dimensionless head contour interval 1/15 and dimensionless stream function contour interval 1/15.

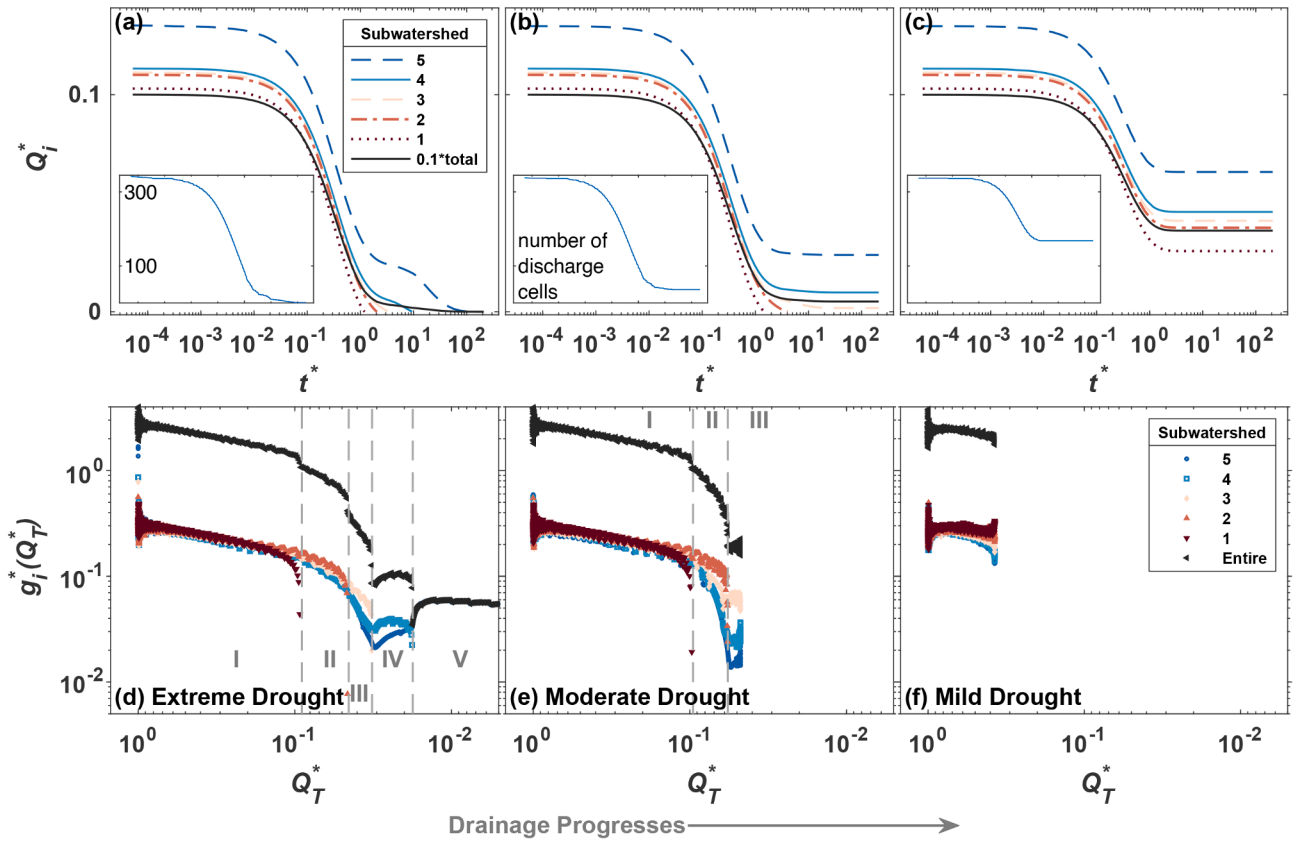

Fig. 3. Temporal evolution of the discharge and the discharge sensitivity function under different drought scenarios (the columns from left to right are extreme, moderate, and mild droughts, respectively). Shown are dimensionless discharge (a)-(c) and discharge sensitivity (d)-(f) for different subwatersheds. The inset plots in the first row use the same logarithmic time scale to show the temporal evolution of the number of discharge cells (out of a possible 676). Note that dimensionless discharge Q_T^* in (d)-(f) represents twice the discharge from the entire modeling domain, as a proxy for the storage in the entire domain (see the last paragraph of Section 2.8 for its definition and reasoning). The dashed vertical lines in (d) and (e) mark the disconnections of water table from subwatersheds and separate different drainage/recession stages I-V.

which mimic local topographic relief (Figs. 2a and 2b, S2a and S2b, S3) and are less influenced by the watershed-scale water-table slope. This leads to similar discharge processes from different subwatersheds, as discussed in the paragraph above. However, at later stages of the drainage (Figs. 2c-2o, S2c-S2i), or for watersheds with relatively large watershed-scale topographic slope (not shown), the GWFS is influenced more by the watershed-scale water-table slope (Fig. S4b). In this situation, baseflow generation becomes scale-dependent and distinct recession behaviors occur for upstream and downstream subwatersheds. This is because, despite the potentially similar local water-table undulations and local flow cells, drainage locations of upstream and downstream subwatersheds tap different positions (e.g., downwelling and upwelling flow regions) of the deeper watershed-scale groundwater flow field, and thus have different discharge patterns.

After the disconnection of water table from subwatershed 4 under the extreme drought, the discharge sensitivity of subwatershed 5 stays nearly constant as discharge further decreases and mimics the discharge recession behavior of a linear reservoir (stage V in Fig. 3d). In fact, during this period of the drainage, the water table has little local undulation and the groundwater flow is primarily driven by the essentially-horizontal hydraulic–head gradient induced by the large-scale remnant watershed-scale water-table slope (Figs. 2m-2o, S4). The groundwater flow during this period can be approximately described by a linearized Dupuit-Boussinesq equation (Brutsaert and Nieber, 1977; Troch et al., 2013).

The above analysis indicates that, in watersheds with a multiscale GWFS, baseflow generation cannot be viewed as simply occurring within hillslopes or conceptualized as drainage from hillslopes overlying horizontal or inclined impermeable bedrocks. Deep groundwater circulation through the large, watershed-scale flow system can lead to different baseflow generation behaviors (e.g., baseflow discharge rate or solute concentration) for upstream and downstream subwatersheds, as is supported by evidence from natural watersheds (e.g., Frisbee et al., 2011; Frisbee et al., 2017; Peralta-Tapia et al., 2015; Ameli et al., 2018; Asano et al., 2020). Furthermore, the importance of the large scale groundwater flow paths increases as the watersheds become drier, such as in late recession stages or in arid regions. Existing observation-based baseflow recession studies focus mostly on relatively short recession time scales and narrow discharge ranges (e.g., recession between rainfall events or seasons; Kirchner, 2009; Teuling et al., 2010; Ajami et al., 2011). So oftentimes only a relatively simple segment of $g(Q)$ is observed. But we need to be cautious if we attempt to use the observed simple $g(Q)$ segment beyond the Q observation ranges, since as shown by our results, dramatic changes of the functional form of $g(Q)$ can exist due to the evolving relative importance of flow paths of different scales.

3.1.3. *Effect of Water-Table Disconnection and GWFS Reorganization on Baseflow Recession*

Disconnections of water table from the land surface in lower-order subwatersheds are accompanied by abrupt changes of the discharge sensitivity, $g_i^*(Q_T^*)$, of the higher order subwatersheds (Fig. 3d and 3e). Specifically, before drainage stage IV under the extreme drought (Fig. 3d) and and drainage stage III under the moderate drought (Fig. 3e), the slopes of discharge sensitivity of downstream subwatersheds increase when water table disconnects from upstream subwatersheds. The disconnection of water table from subwatersheds does

not occur for the mild drought.

These phenomena happen because the water-table disconnections from subwatersheds cause abrupt changes in the pattern of water-table evolution and the reorganization of the GWFS. We use disconnections of the water table from subwatershed 1 under the extreme and moderate droughts to elaborate this point (Figs. 2a-2d, S2a-S2d). Before the disconnection of water table from subwatershed 1, the drainage is accompanied by the lowering and flattening of the local water-table mounds between drainage regions of neighbouring subwatersheds. The local water-table mounds induce separate local flow cells, transporting water toward drainage regions on the two sides of each water-table mound (Figs. 2a-2c, S2a-S2c). The larger, watershed-scale shape of the water table is barely influenced because the water table is pinned at the drainage regions in each subwatershed (i.e., a topographic constraint on the water table). The drainage and baseflow recession behavior, as reflected by the discharge sensitivity function, evolve gradually and smoothly during the time period before the first disconnection at the end of drainage stage I (Figs. 3d and 3e). When the water table disconnects from subwatershed 1, the two local-scale components of the GWFS on the two sides of outlet 1 disappear and the local flow field near outlet 1 becomes part of the larger, watershed-scale flow component (Figs. 2c and 2d, S2c and S2d). The water table between outlets 1 and 2, and the water table upstream of outlet 1, now evolve together. Water-table disconnections from subwatersheds change the shape of the larger, watershed-scale water table and reorganize the GWFS, thus perturbing baseflow recession behavior in downstream subwatersheds.

These phenomena indicate that, in watersheds where multiscale GWFSs exist (e.g., mountainous watersheds with deep and permeable bedrock), flow cells of the GWFS supplying baseflow to individual subwatersheds interact with one another. Baseflow generation in different subwatersheds should not be treated as being independent.

3.2. *Baseflow Residence Time and Groundwater Age Under the Extreme Drought Scenario*

Joint analysis of baseflow recession from both a groundwater hydraulic perspective (by analyzing the groundwater flow field, baseflow discharge, and storage-discharge relationship) and a solute transport perspective (by analyzing groundwater age, baseflow residence time, and selective drainage of water of different ages) provides a more holistic view of the watershed's functioning in storing and releasing water and solutes (McDonnell and Beven, 2014). Discharge is driven by the instantaneous hydraulic head (potential energy) gradient of water stored in the watershed. Discharge sensitivity tells us the relative magnitude of discharge change caused by the change of storage and potential energy gradient which are a result of the net flux in/out of the watershed. Discharge and discharge sensitivity provide measures of the hydraulic response of the watershed, but contain no information about the evolving baseflow source and water quality. Baseflow residence time distribution, RTD, measures the age composition of water parcels in the baseflow and indicates whether baseflow comes from nearby riparian zones/hillslopes arriving through short flow paths or from faraway mountains arriving through long and deep flow paths, or both. Baseflow RTD together with the age distribution of groundwater in storage indicate how watersheds selectively drain groundwater of different ages from flow paths of different scales. Baseflow RTD and groundwater-age distribution analyses provide an explicit view of how the multiscale GWFS influences baseflow generation and elucidates the important role of deep groundwater circulation. Here we examine these issues in detail for the case of an extreme drought with no recharge.

3.2.1. *Spatiotemporal Evolution of Groundwater Age*

The spatial distribution of groundwater age at the beginning of the drainage shows distinct age zones associated with the local (and watershed-scale) flow paths induced by the local relief amplitudes (and the watershed-scale topographic slope) (Fig. 4a). The local-scale GWFS components are mainly composed of relatively young water and have similar spatial patterns of groundwater age in different subwatersheds. This is a result of the similar steady-state groundwater flow patterns in the local flow cells at the beginning of the drainage due to the same climate condition, local relief, and homogeneous hydraulic conductivity (Fig. 2a). However, due to the downwelling of the deep, watershed-scale flow field near the headwater (and upwelling near the main stream), the young age zone of local-scale flow cells near the headwater extends deeper into the modeling domain than those near the main stream (e.g., Fig. 4a).

The water flowing through the deep, watershed-scale flow field ages from the headwater to the main stream (Fig. 4). This is trivially true, but has significant implications for understanding baseflow generation and source at the watershed scale. The portion of baseflow contributed by the local-scale flow cells may have similar RTD at different subwatersheds. However, the portion of baseflow contributed by the deep, watershed-scale flow field can have very different RTD for upstream and downstream subwatersheds (e.g., increasingly heavier tail at large residence time from upstream to downstream), as is discussed in the following section. The deep, watershed-scale flow cell has been hypothesized as a direct contribution to the observed water aging and increasing baseflow mineral-solute concentration from upstream to downstream in natural watersheds with deep and permeable bedrock, indicating the importance of deep groundwater circulation in streamflow generation and conceptualization (e.g., Frisbee et al., 2011; Frisbee et al., 2017; Peralta-Tapia et al., 2015).

During the entire drainage process, the GWFS experiences aging and the local-scale flow cells are stretched downstream by the deeper, watershed-scale flow field (Fig. 4). But the main spatial pattern of groundwater age inherited from the initial steady-state groundwater flow field is preserved. This age pattern, as determined by past hydrological conditions before the drainage, marks the organization and evolution of the GWFS and explains the evolving baseflow RTD during the drainage (Section 3.2.2).

Due to factors such as hydrogeologic heterogeneity, topographic complexity, spatial variations and intermittency of precipitation events, and climatic variations at different spatial–temporal scales, the spatial pattern of groundwater age at the beginning of baseflow recession in natural watersheds is typically more complex than what is presented in Fig. 4a. However, we are not attempting to reproduce the complex groundwater-age distribution and baseflow RTD observed in natural watersheds. Rather, we use groundwater-age distribution and baseflow RTD as indicators/markers for the evolution of the multiscale components of the GWFS in order to reveal their role in baseflow generation. We focus on the relationships between the multiscale GWFS and baseflow generation, rather than the detailed composition of the water. Our conclusions don't depend on the specific patterns of groundwater-age distribution or baseflow RTD, which are manifestations of the accumulated effect of recharge, subsurface mixing, and discharge that the watershed has experienced in the past. Even for a system with more complex age patterns and more complex baseflow RTD, the timing and proportion of the contribution of the multiscale components of the GWFS to baseflow and baseflow recession behavior are determined by the system hydraulic conditions at the beginning of and during the drainage process, rather than by the specific patterns of groundwater-age distribution or baseflow RTD, which are formed during the history of the watershed before the recession event.

The fully-saturated steady-state groundwater flow field used as the initial condition for the drainage in our model can represent a long-term average groundwater flow condition. This is particularly true in a humid watershed where the groundwater table closely follows land-surface topography. But it also can apply to semiarid climates with enhanced recharge at higher elevations (Wilson and Guan, 2004; Stephens and Umstot, 2019). The initial groundwater-age pattern, although simple and lacking of the more detailed age patterns induced by complex

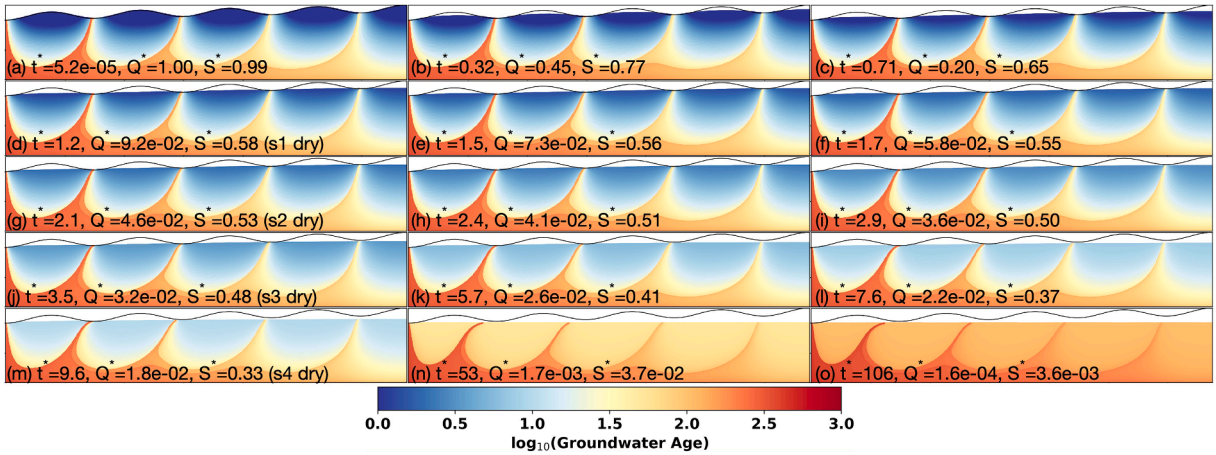

Fig. 4. Spatiotemporal evolution of the groundwater age. Spatial distribution of dimensionless groundwater age at selected time instants t^*, shown in the labels, for the extreme drought scenario. The same time instants are used as in Fig. 2. Plots (d), (g), (i) and (m) correspond to the disconnections of the water table from the subwatersheds from upstream to downstream, as indicated in the labels by '*si* dry' ($i = 1, 2, 3, 4$). The dimensionless groundwater age for particles remaining in the domain at any time instant is the time lapse since the entrance of the particle into the domain. The details of the age estimation method are in Section 2.5. The dimensionless discharge Q^* and dimensionless storage S^* are also shown in the labels to indicate the drainage state of the system.

meteorological perturbations and subsurface mixing, represents the overall long-term average age pattern. The relatively simple age pattern associated with flow cells of different scales clearly marks and delineates these different flow cells and traces the role of the GWFS in baseflow generation, which serves to meet our research purpose. Although adding more complexity might reveal more interesting subsurface mixing phenomena, the specificity of the complexity is not relevant to our research purpose and can obscure the generality we want to achieve in this study.

3.2.2. *Evolution of Baseflow Residence Time Distribution and Sources*

The temporal evolution and spatial patterns of groundwater age is directly related to the evolution of baseflow RTD (Figs. 5 and S9). During the first stage of the drainage (i.e., from the beginning of the drainage to the disconnection of water table from subwatershed 1), subwatersheds 1–3 have very similar baseflow RTD (Figs. 5(a-c)I and S9). The similarity in RTD is a result of the similar spatial patterns of the GWFS directly supplying baseflow to subwatersheds 1–3 (Figs. 2a-2c, 4a-4c). The RTD is characterized by one mode spanning young residence times. This is caused by the dominating contribution of local-scale flow paths to baseflow (Figs. 4a-4c and 8a). As can be seen from the baseflow source areas annotated by *i*-I ($i = 1, 2, 3$) in Fig. 8a for this first drainage stage, baseflow is primarily contributed by young groundwater beneath the drainage area. As a result of the downstream aging and increasing contribution to baseflow of water flowing through the regional-scale flow paths, the RTDs from higher-order subwatersheds have longer tails at large residence times (Figs. 5d-I and 5e-I), although the overall shape of the RTDs is similar to that for subwatersheds 1–3. However, a gap (i.e., a horizontal segment) in the RTDs and a jump following the gap can be found around a residence time of $100t_c$. This is because subwatersheds 4 and 5 directly tap the upwelling region of the deep, watershed-scale flow field and gain a larger proportion of baseflow from the old water in that flow field (Figs. 4a-4c and 8a). The temporal change of RTDs is small during the first stage of the drainage, but with a slight shift of the mode toward younger residence times (Figs. 5(a-f)I and S9). This indicates an increasing proportion of younger baseflow from local-scale flow cells.

During the second stage of the drainage, the shape and the evolution patterns of RTD for subwatersheds 2–4 (Figs. 5(b-d)II) are similar to that during the first drainage stage. However, RTD for subwatershed 5 shows an increase in the weight of the mode at a residence time of about $300t_c$ (Fig. 5e-II), indicating an increasing proportion to baseflow from regional-scale flow paths (Fig. 8a). During stages III-V of the drainage, the temporal evolution of RTD for subwatersheds 4 and 5 is dominated by the natural aging of groundwater, as indicated by the shift of the RTD toward large residence times (Figs. 5d-III, 5d-IV, 5e-III, 5e-IV and 5e-V). The relative probability mass covered by the two modes at relatively young and old residence times changes little, as shown by the unchanging vertical rises of the RTD curves preceding and following the horizontal gap at around $100t_c$ (e.g., Fig. 5e-IV). This indicates that the relative contribution to baseflow by local- and regional-scale flow paths is stable, probably due to the stable relative magnitude of the flushing intensity of the local- and regional-scale flow cells at this late stage of the drainage (Fig. S4a).

The evolution of baseflow RTD (Figs. 5 and S9) reveals the changing proportions of young/old groundwater in supplying baseflow caused by the reorganization and changing relative strengths of flow cells of different scales in the GWFS (Figs. 2 and S4). Unlike the discharge sensitivity, no abrupt changes of RTD occur when the water table disconnects from the various subwatersheds (Fig. 5). A hydraulic perturbation is revealed immediately in water discharge and solute export rate (McDonnell and Beven, 2014). But the solute composition of discharge, as indicated by RTD, is determined by both the composition of water available to be discharged and the proportion of discharge from water of different compositions in storage. One way to describe the selective discharge of groundwater of different compositions is the storage selection (SAS) function, Eq. (20) (e.g., Harman, 2015). Contrasting Fig. 4c with 4d, 4f with 4g, 4i with 4j, and 4l with 4m shows that there are no immediate or dramatic changes of groundwater age or its spatial pattern when the water-table disconnections occur. So the relatively stable RTD before and after a water-table disconnection indicates that the SAS function is not dramatically perturbed at the time of a water-table disconnection.

Although water-table disconnections do not cause sudden changes of SAS functions and flow paths, the water-table disconnection and the accompanied GWFS reorganization cause the evolution of flow paths to be different from that before the disconnection, which is reflected in the different evolution schemes of RTD before and after water-table disconnections (e.g., compare Fig. 5d-II with 5d-III, 5e-I with 5e-II, and 5e-II with 5e-III). This is especially true for high-order subwatersheds.

The different RTD evolution schemes are related to the changes in baseflow sources due to the evolution of the multiscale GWFS. Baseflow during different stages of the drainage is mainly from groundwater storage close to the drainage areas (Fig. 8a), rather than entirely from hillslope storage that assumes an impermeable bedrock underlying hillslopes (e.g., Fig. 2 in Pauritsch et al., 2015). During the first stage of

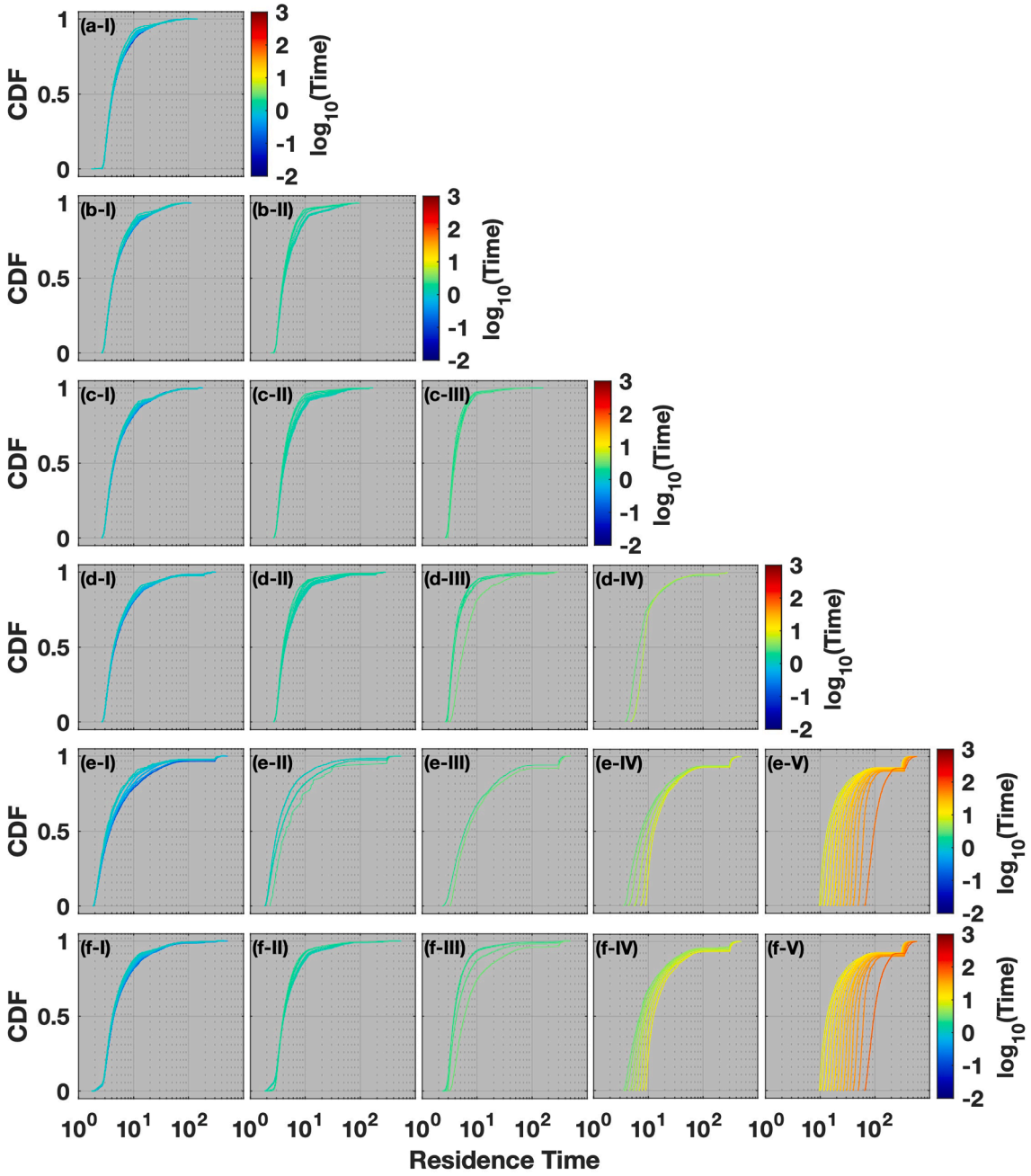

Fig. 5. Baseflow residence time distribution. Temporal evolution of baseflow dimensionless residence time distribution (RTD) from subwatersheds 1–5 (a-e) and the entire 2-D domain (f) under the extreme drought scenario with zero recharge, presented as cumulative distribution functions (CDF). For easier inspection, CDFs are shown separately for drainage stages (I-V) between the disconnections of water table from subwatersheds. The time (color bar) is also shown in dimensionless form. Fig. S9 in the Supporting Information collects the RTD during different drainage stages all in one plot for each subwatershed to show the RTD evolution during the entire modeling period.

the drainage, baseflow is mainly from storage below the drainage areas of each subwatershed (zones labeled *i*-I in Fig. 8a, for $i = 1,2,3,4,5$). A large proportion of the drained storage is from the local flow cells and a small proportion is from the upwelling of the larger, watershed-scale flow cell into subwatershed 5 (Fig. 8a). The evolving proportions and timing of water drained from local and watershed-scale flow cells contribute to the evolution scheme of baseflow RTD (Figs. 5(a-e)I). As the drainage progresses, the source regions for baseflow expand radially outward from each of the drainage areas (Fig. 8a). For subwatersheds 1–4, the storage near and below the peaks of the hills never drains out as local baseflow from these subwatersheds, but instead, as the water table drops, flows deeper into the domain and becomes part of the deep, watershed-scale component of the GWFS (Fig. 2). This portion of water storage eventually subsidizes the main stream, as is also indicated by observations and modeling in natural watersheds (Manning and Solomon, 2005; Manning, 2011; Rumsey et al., 2015; Ameli et al., 2018). Also notice that, due to the bias of the groundwater-watershed divides toward the upstream direction under the influence of the watershed-scale water-table slope (Fig. 2), hillslopes of the same shape on the two sides of the stream don't contribute equally to baseflow (Fig. 8a).

3.3. Baseflow Residence Time and Groundwater Age Under the Moderate and Mild Drought Scenarios

The shape and evolution patterns of RTD under the moderate and mild drought scenarios differ from that under the extreme drought mainly in the late drainage period, as the flow fields under different drought scenarios asymptotically approach different steady-state flow fields (Figs. 5–7). For these two less-severe drought scenarios, the complexity of the final steady-state baseflow RTD increases from upstream to downstream (Figs. 6 and 7). Moreover, both the moderate and mild droughts produce more complex final steady-state RTDs than does the extreme drought, as is reflected by the number of modes in the RTD's approaching final steady states (Figs. 5–7). Under the moderate and mild droughts, flow paths of a wide range of scales all play important roles in contributing to baseflow, especially at the late period of the drought and/or in higher-order subwatersheds, while during the early period of a drought or for lower-order subwatersheds, local-scale flow cells dominate the contribution to baseflow and thus produce less complex RTDs.

During the first drainage stage under the moderate drought, the spatial distribution of baseflow sources is similar to that under the extreme drought (Figs. 8a and 8b). Baseflow is entirely contributed by water in storage that is recharged before the start of the drought. For both the moderate and extreme droughts, the second drainage stage under the drought is defined as the time interval between the disconnections of water table from subwatershed 1 and 2. However, compared to the extreme drought, more young water in storage contributes to baseflow during the second drainage stage under the moderate drought (Figs. 8a and 8b). This is because the second drainage stage under the moderate drought ($t^* \in [1.5, 4.1]$, see plot label in Fig. S2) persists for a much longer time than does the second drainage stage under the extreme drought ($t^* \in [1.2, 2.1]$, see plot label in Fig. 2). The slower-declining water table sustained by the recharge drives more young water out of the domain as baseflow.

For higher-order subwatersheds during the third drainage stage under the moderate drought (Fig. 8b), and during the entire drainage stage under the mild drought (Fig. 8c), a significant amount of groundwater contributing to baseflow to individual subwatersheds is from inter-subwatershed upstream regions. This explains the complex baseflow RTD during these drainage stages (Figs. 6 and 7).

During the second and third drainage stages under the moderate drought and during the entire drainage stage under the mild drought, baseflow is contributed by both water in storage at the beginning of the drought and new recharge occuring after the beginning of the drought (bottom and top parts, respectively, of the panels shown in Figs. 8b and 8c). For any one specific subwatershed, new recharge from both within and without the subwatershed contributes to baseflow. The multiscale GWFS breaks the barriers of the topographic divide between subwatersheds and makes baseflow source identification, discharge, and water quality prediction much more complex.

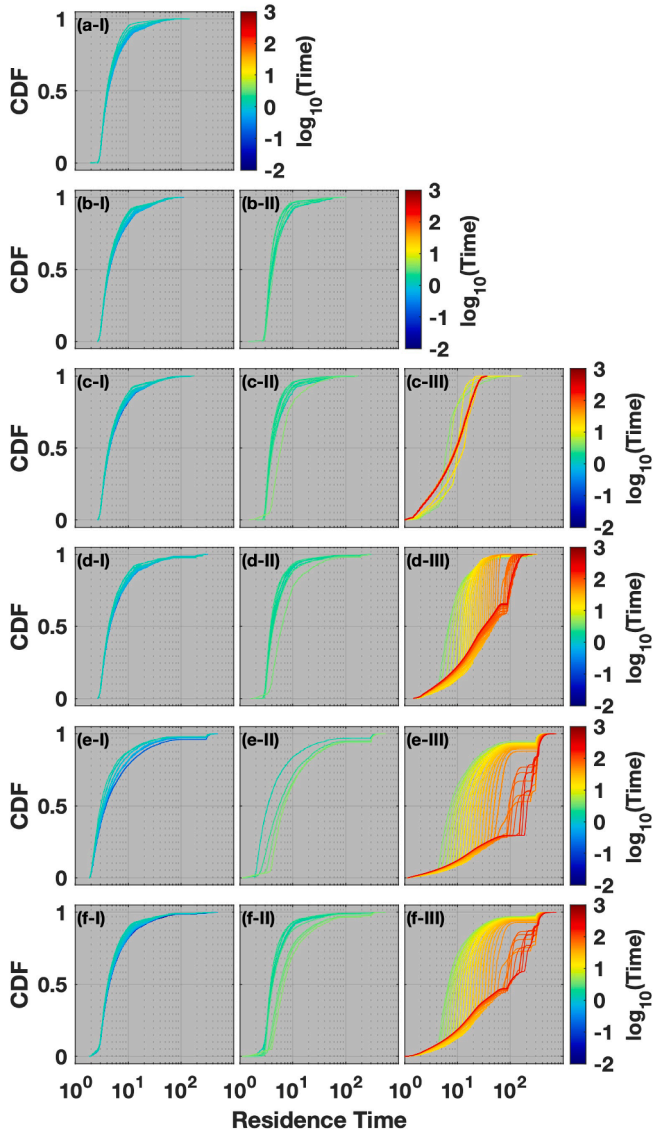

Fig. 6. Similar to Fig. 5 but for the drainage under a moderate drought with a recharge rate of 14.8 mm/yr. Fig. S10 collects the RTD during different drainage stages all in one plot for each subwatershed.

3.4. Implications for the Conceptualization of Baseflow Generation

The conceptualization of baseflow generation is widely used to interpret baseflow recession behavior and identify controlling factors, infer watershed hydrogeologic and geomorphic parameters based on discharge observations, and parameterize the baseflow component in conceptual hydrological models. When using hydraulic groundwater theory (see, e.g., Troch et al., 2013 for a review) to interpret baseflow recession behavior and infer watershed-scale equivalent hydrogeologic parameters, it is traditionally assumed that discharge from the entire watershed is a simple aggregation of simultaneous discharging processes from identical hillslopes arranged in parallel along the stream network (Brutsaert and Nieber, 1977; Rupp and Selker, 2006). Harman et al. (2009) relax the "identical hillslope" assumption and show that the heterogeneity of recession time scales of individual hillslopes can generate the range of recession slope curves observed in nature. However, Harman et al. (2009) still conceptually assume that individual hillslopes are arranged in parallel and have no interactions with each other. Our results from physically-based modeling clearly demonstrate that baseflow discharge processes from different hillslopes or different subwatersheds are not independent if they are supplied by a multiscale GWFS where flow paths of multiple scales can interact with each other.

Biswal and Marani (2010) relate watershed stream network structure to baseflow recession characteristics, moving one step forward beyond the traditional focus on hillslope scale dynamics while studying baseflow generation. They show the relation between the contraction of an active drainage stream network and watershed-scale baseflow recession characteristics under the following assumptions. (1) Baseflow during recession varies slowly in time and can be described by a succession of steady states. (2) Discharge processes from hillslopes along unit-width stream segments are identical (in their words, spatially constant). (3) Active stream heads recede at constant speed. A close examination of the second and third assumptions reveals some contradiction. If discharge processes from hillslopes are spatially constant (i.e., identical and synchronized), then how can the stream network dry up gradually from

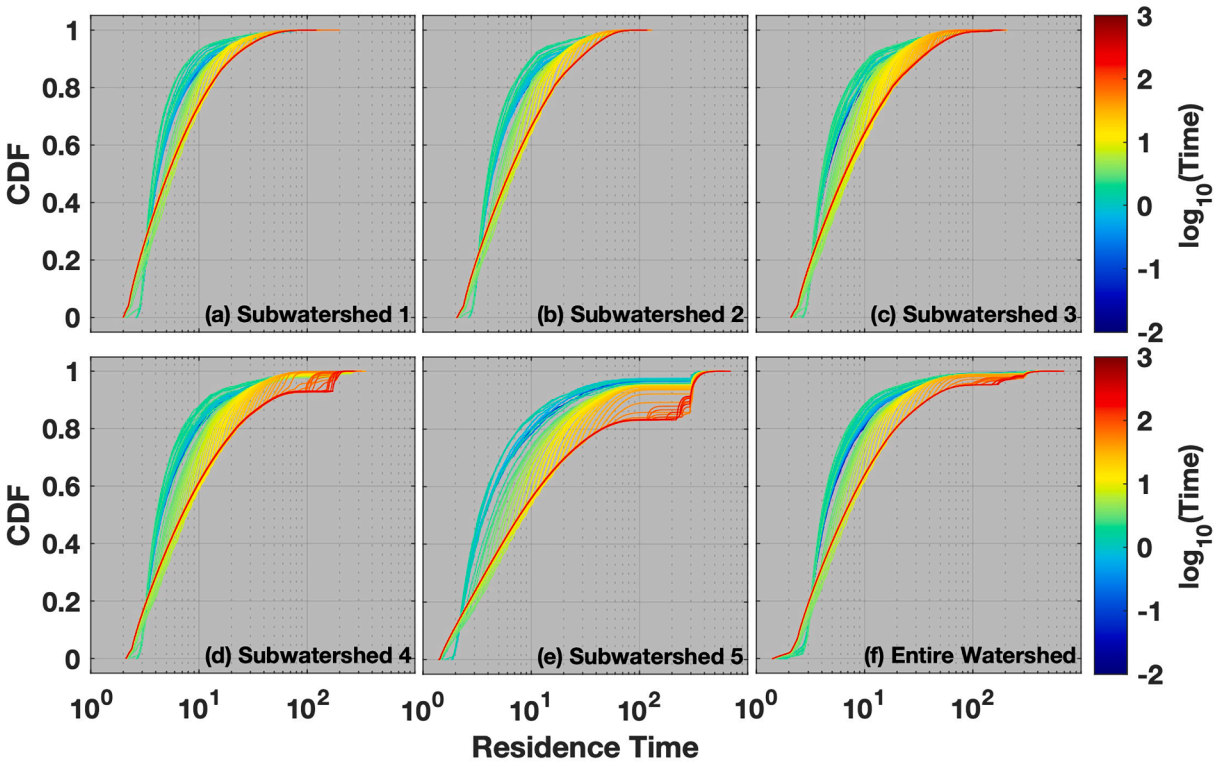

Fig. 7. Similar to Fig. 5 but for the drainage under a mild drought with a recharge rate of 148.0 mm/yr.

upstream to downstream? Different segments of the entire stream network should dry up at the same pace when the discharge into all stream segments approaches zero synchronically. Based on our results and some additional thought experiments, the most questionable assumption, which leads to the contradiction, is the second one that assumes that discharge into per-unit-length stream segment is spatially constant. This assumption of "being spatially constant" prohibits the study of the impact of any "spatial structure" on baseflow recession. Their first assumption remedies the contradiction. All three assumptions together actually conceptualize watershed-scale baseflow recession as the successive and sudden shutting down of discharge from unit-width stream segments along the stream network from upstream to downstream. If we conceptualize the water table in a watershed as a connected entirety, with the stream-water stage being the groundwater water table in the stream (e.g., Winter et al., 1998), then the receding of active stream heads during the dry season is a manifestation of the lowering of water table at the watershed scale, which is "likely to occur in sloping basins" (as stated by Biswal and Marani, 2010). Thus, recognizing the importance of the dynamics of the multiscale GWFS, in addition to the dynamics of baseflow from individual hillslopes, is essential for understanding the control of watershed-scale geomorphological structure on baseflow generation and recession behavior (e.g., Wang et al., 2018).

The assumptions used in the above cited studies are more appropriate for watersheds with shallow impermeable bedrock and gentle watershed-scale topographic slope. The role of nested multiscale GWFS is rarely considered in baseflow generation studies. Our modeling suggests that assuming discharge processes from hillslopes to be identical and independent is likely inappropriate for watersheds with deep and permeable bedrock and multiscale topographic relief (e.g., Frisbee et al., 2017; Ameli et al., 2018). These types of watersheds are often found in mountainous headwater regions with fractured bedrock (Wilson and Guan, 2004; Gleeson and Manning, 2008; Welch and Allen, 2014). The interactions of multiscale components of the GWFS and their evolving role in baseflow generation can make the baseflow generation behavior significantly different from that of individual hillslopes or aggregations of hillslopes. In a 3-D watershed, topography is hierarchically organized, with lower-order subwatersheds overlying and embedded in higher order subwatersheds. The hillslopes of subwatersheds of different orders usually have different wavelengths, amplitudes and orientations (Rodríguez-Iturbe and Rinaldo, 1997; Perron et al., 2008). Under ideal climatic and hydrogeologic conditions, the water table can be a subdued imitation of the land-surface topography (e.g., Tóth, 1963; Freeze and Witherspoon, 1966). The water table relief thus shares the multiscale nature of the land-surface topography and can be viewed as a linear combination of undulations at different spatial scales, with different amplitudes and orientations (e.g., Wörman et al., 2006; Wörman et al., 2007). The water-table gradient beneath the hillslopes and the underlying 3-D groundwater flow directions do not have to be along the sloping directions of the lowest order hillslopes. The influence of the evolving watershed-scale water-table relief must be taken into account when interpreting baseflow recession at the watershed scale and building conceptual baseflow models.

In many rainfall-runoff models, baseflow generation is conceptualized as discharge processes from single or multiple reservoirs arranged sequentially or in parallel, and is parameterized as linear or nonlinear storage-discharge relationships (e.g., Gelhar and Wilson, 1974; Clark et al., 2008; Luo et al., 2012; Stoelzle et al., 2015). Our results show that baseflow generation behavior, as characterized by the storage-discharge relationship, is not static but changes as the watershed wetness condition changes. Moreover, even with the same local hydrogeologic and geomorphic conditions, subwatersheds with different deep, watershed-scale, or even inter-watershed-scale groundwater flow conditions can have significantly different baseflow generation behavior. In other words, the baseflow generation behavior of individual watersheds is determined not only by their within-watershed landscape and climate conditions, but also influenced by the landscape and climate conditions of the higher order watersheds encompassing them. This calls for caution in the regionalization of rainfall-runoff model structures to ungauged basins based only on physiographic and/or meteorological

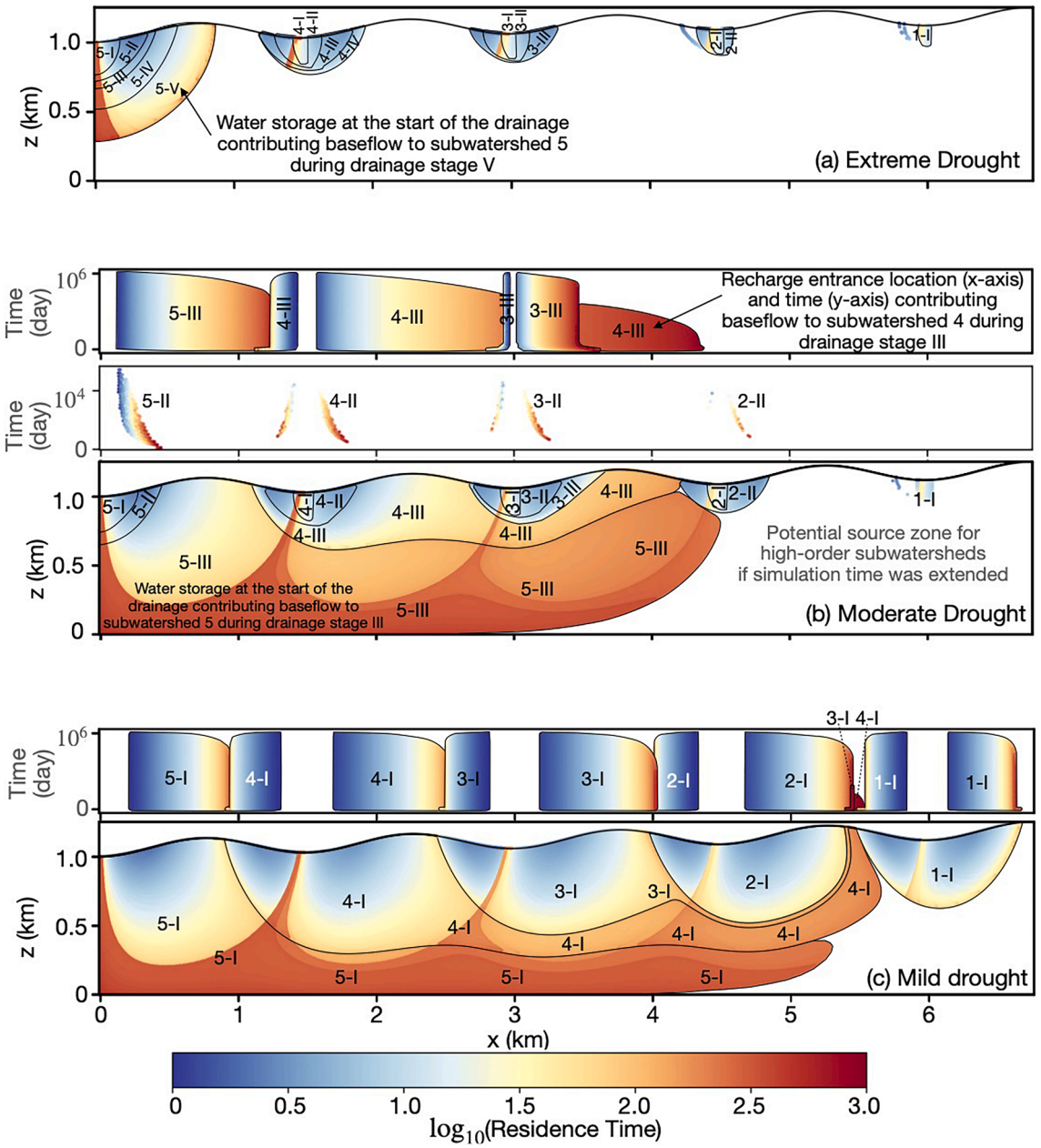

Fig. 8. Sources of baseflow to different subwatersheds during drainage stages between consecutive water table disconnections, as identified by particle tracking, for the three drought scenarios. Each source zone is labeled by an Arabic numeral indicating the target subwatershed and a Roman numeral indicating the drainage stage. In the lower part of each panel, the color patches are composed of water parcels drained out as baseflow plotted at their locations within the domain at the start of the drainage. The upper part of each panel shows the entrance time (vertical axis) and location (horizontal axis), and the dimensionless baseflow residence time (color scale), of water parcels that entered the domain after the start of the drainage but also drained out as baseflow during the corresponding drainage stage. The color indicates dimensionless baseflow residence time for each particle as it discharges from the groundwater. Blank areas on the right lower part of panels (b) and (c) would eventually become baseflow sources to high-order subwatersheds if the simulation time was extended.

attributes (e.g., Yadav et al., 2007; Santhi et al., 2008).

3.5. Simplifications, Limitations, and Future Study

A 2-D sinusoidal topography with a linear regional slope is used for our model domain. This topographic configuration, although simple, incorporates the general undulating and multiscale features of natural topography and drives the formation of a multiscale GWFS with nested flow paths. Adding complexity to the topography can correspondingly increase the complexity of the groundwater flow field, but will also make the topography, and thus the topography-driven groundwater flow field, more unique and specific to a certain type of landscape, and make the conclusions less universal and harder to transcend place.

Compared to 2-D cross-sectional models, 3-D watershed models can incorporate the 3-D features of landscapes, such as the stream network and diverse hillslope plain-view shapes, and can simulate more complex 3-D groundwater flow fields. Baseflow recession behavior influenced by stream network patterns, and the interaction between groundwater table and 3-D topography (e.g., the drying up of the stream network; Godsey and Kirchner, 2014), should be studied in the future.

The homogeneous hydraulic conductivity field used in our simulations does not incorporate geological features such as a shallow highly permeable soil and weathered bedrock, a change of bedrock permeability with depth (e.g., due to compression), hydrostratigraphic

layering, or structural features such as faults. We choose to use a single homogeneous hydraulic conductivity scenario for three reasons. First, a shallow highly permeable zone is important to baseflow generation in some, but not all, natural watersheds. There are also many places where shallow soil and highly weathered bedrock is uncommon or do not exist. For example, bedrock watersheds with no unconsolidated soils are common in the Western US, such as the Sierra Nevadas and the coastal ranges of California (e.g., the sandstones of the Santa Ynez Mountains). Watersheds with little weathered bedrock at the top are also common in the carbonates of Florida and Door County, Wisconsin. In any event, the conditions simulated here are also equivalent to hilly terrain with silty sands, silt, loess, or glacial till aquifers, even without rescaling. Second, our focus is on the contributions of deeper components of the GWFS to baseflow, including the flow paths at the scales of hillslopes and deeper flow paths at larger inter-subwatershed and watershed scales. Although we simplify the shallow soil and weathered bedrock zone, we do consider a wide spectrum of flow paths from hillslope scale to watershed scale. Third, using a single hydraulic conductivity scenario also helps us to better focus on demonstrating and improving our mechanistic understanding of the role of multiscale groundwater flow paths in watershed-scale baseflow generation. A shallow highly permeable zone could allow preferential groundwater flow at the early stage of the drainage and potentially further distinguish the contributions of shallow and deep flow paths to baseflow. Our modeling and analysis framework can be extended in the future to implement a depth-decaying permeability profile that potentially addresses some of these issues.

4. Summary, Conclusions and Implications

In this paper, we study baseflow generation and recession behavior in watersheds with deep and permeable bedrock. This special landscape setting favors the development of a groundwater flow system (GWFS) with deep, as well as shallow, flow components, which can play an important role in stream baseflow generation. We analyze numerically simulated baseflow generation and the GWFS in a 2-D cross section of an idealized watershed for three different prolonged droughts, leading to three different examples of water table disconnections from subwatersheds. Baseflow discharge and residence time distribution (RTD), as well as the groundwater flow field and groundwater-age distribution, are analyzed to understand the dynamics of baseflow and the multiscale GWFS during prolonged droughts (Fig. 9). The changes of baseflow discharge sensitivity and RTD, as indicators of watershed-scale baseflow generation and solute export characteristics, are explained by the evolution of the groundwater flow field, the interactions among flow components of different scales in the GWFS, and the evolving shape and position of water table and its disconnections from subwatersheds (Fig. 9).

Based on our analysis, we conclude that flow paths of different spatial and temporal scales of the GWFS interactively influence baseflow generation but with distinct and evolving roles during the sequential stages of the drainage and for each subwatershed, depending on the relative strength of the flow paths, and the relative positions of the subwatersheds to the recharge/discharge zones of the watershed-scale flow paths. During the early stage of the drainage, baseflow recession in all subwatersheds is primarily influenced by the local subwatershed-scale flow paths which contribute young water originating from recharge in the nearby hillslope areas to the baseflow. The baseflow discharge sensitivity function has a power-law form, which matches the behavior recorded by field observations. As the drainage progresses, the lowering of the water table, the flattening of local water table undulations, and the disconnection of water table from subwatersheds diminish local subwatershed-scale flow paths and their relative importance in shaping baseflow recession behavior. During this period of the drainage, the watershed-scale deep component of the GWFS takes more and more control of baseflow generation, contributing a larger proportion of older water to baseflow and leading to more complex baseflow recession behavior.

As the drainage progresses the evolving multiscale components of the GWFS, and their changing relative strength and contribution to baseflow generation, lead to increasingly dissimilar baseflow discharge

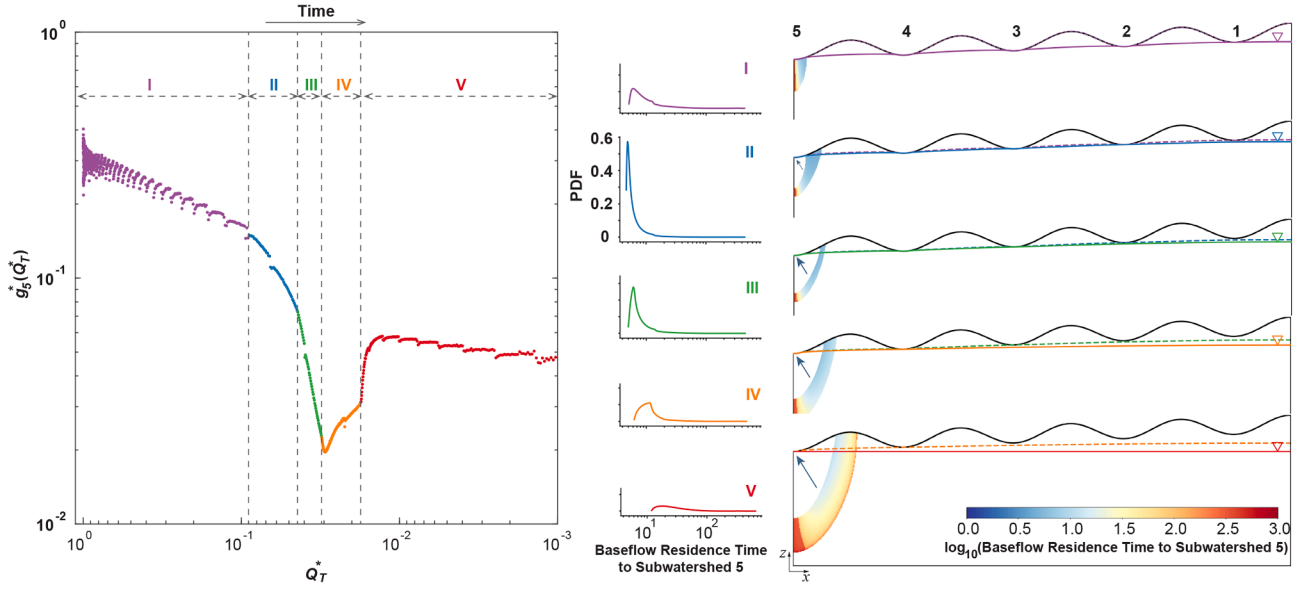

Fig. 9. Summary of this study's analysis framework using the extreme drought and subwatershed 5 to illustrate. Groundwater discharge and solute export processes are characterized by the evolution of dimensionless discharge sensitivity (a hydraulic perspective; left column) and probability density function of dimensionless baseflow residence time (a transport perspective; middle column). The underlying physical mechanisms are attributed to the evolution (Stages I-V) of the shape and position of water table and baseflow source region (right column). In the left column, Q_T^* is twice the dimensionless discharge from the entire modeling domain Ω (Section 2.8). $g_5^*(Q_T^*)$ is the dimensionless discharge sensitivity of subwatershed 5. In the right column, the dashed and solid curves represent the initial and final water table positions during each of the selected time periods of drainage. The colored patches are composed of the drained water parcels at their locations at the beginning of the drainage and the color of the patch shows their dimensionless baseflow residence time when they discharge to the surface. These young and old water parcels are transported by local shallow short and regional deep long flow paths, respectively, to their plotted locations at the time when the drainage starts.

sensitivity and RTD from different subwatersheds despite their similar landscape and climate conditions and produce spatial scale-dependent baseflow generation behavior. During the early stage of the drainage, the local subwatershed-scale components of the GWFS have similar hydraulic head and age patterns, due to the same local topographic relief, climate and geology. This similarity in early stage subwatershed-scale flow component contributes to similar discharge recession behavior and RTD of baseflow from lower-order subwatersheds. The highest-order subwatershed is strongly influenced by the deep, watershed-scale component of the GWFS and has the most distinct RTD patterns during the early stage of the drainage. The different positions of subwatersheds, relative to watershed-scale downwelling and upwelling flow zones, strengthens the dissimilarity in baseflow recession behavior and RTD among different subwatersheds, especially during the later stages of the drainage. The influence of the deep, watershed-scale component of the GWFS on baseflow generation is most significant in the highest order subwatershed and is evident even in the early stages of drainage. When the watershed topographic slope increases, this scale-dependent influence of the watershed-scale flow component becomes more obvious (not shown) and can have more significant effect on baseflow generation in all subwatersheds even during the early stage of the drainage.

We earlier noted (Section 2.1) that the different drought-induced drainage stages modeled in this study can also be used to represent the average drainage conditions and their responses to droughts for otherwise similar watersheds in different climates. With similar topography and geology, watersheds in drier climates produce older and more chemically-evolved baseflow, as indicated by the final equilibrium RTD under reduced recharge rates. However, baseflow from watersheds in temperate climates has much more complex residence time distribution than baseflow from topographically and geologically similar watersheds in both humid and dry climates. Under a drought, discharge sensitivity of watersheds in drier climates is smaller than that of watersheds in more humid climates. For watersheds in different climates, the sensitivity of baseflow residence time distribution (or, sensitivity of discharge of different residence times) to drought perturbations is worth future study.

Also note that our conceptual model with a homogeneous hydraulic conductivity field corresponds to natural watersheds with deep and permeable bedrock. The heterogeneity of hydraulic conductivity field, such as a depth-decaying K (Ingebritsen and Manning, 1999; Cardenas and Jiang, 2010), can influence the relative contribution of flow paths of different scales to baseflow generation. However, our findings are due to the multiscale nature of the GWFS and should persist even in watersheds with heterogeneous geology, as long as there is a multiscale GWFS with its various subwatersheds having time-varying connections to flow paths of different scales.

Our results call for caution in conceptualizing baseflow generation at the watershed scale as a synchronized or sequential aggregation of baseflow generated independently from individual hillslopes. First, baseflow may not be entirely contributed by water storage within the hillslopes on the two sides of the streams, depending on the depth and complexity of the GWFS. Second, for watersheds with a developed GWFS (e.g., in hilly or mountainous regions with deep and permeable bedrock) the watershed-scale baseflow generation mechanism cannot be represented by a simple aggregation (e.g., multiplication, linear combination, or convolution) of hillslope or subwatershed-scale baseflow generation processes. This is indicated by the asynchrony and dissimilarity of baseflow generation from hillslopes under the impact of the watershed-scale GWFS, and the dynamic interactions among flow components of different scales.

CRediT authorship contribution statement

Chao Wang: Conceptualization, Methodology, Software, Formal analysis, Investigation, Data curation, Writing - original draft, Visualization. **Jesus D. Gomez-Velez:** Conceptualization, Methodology, Resources, Supervision, Funding acquisition, Project administration, Writing - review & editing. **John L. Wilson:** Conceptualization, Methodology, Resources, Supervision, Funding acquisition, Project administration, Writing - review & editing.

Declaration of Competing Interest

The authors declare that they have no known competing financial interests or personal relationships that could have appeared to influence the work reported in this paper.

Acknowledgements

This work was supported through funding from the New Mexico Water Resources Research Institute Faculty Water Research Grant; the National Science Foundation (EAR-1830172, OIA-2020814, EAR-1015100, CNH-1010516, and EAR-0814449); the Consortium for Risk Evaluation with Stakeholder Participation (CRESP), funded by the U.S. Department of Energy under Cooperative Agreement Number DE-FC01-06EW07053; and the U.S. Department of Energy, Office of Science, Office of Biological and Environmental Research, Environmental System Science (ESS) program through a subcontract from the River Corridor Scientific Focus Area project at Pacific Northwest National Laboratory. The opinions, findings, conclusions, or recommendations expressed herein are those of the authors and do not necessarily represent the views of the Department of Energy or Vanderbilt University. We thank Prof. Fred Phillips and Kyungdoe Han at New Mexico Tech for reviewing and offering helpful comments and suggestions. We greatly appreciate the comments from the editor, the associate editor, and the anonymous reviewers.

Appendix A. Supplementary data

Supplementary data associated with this article can be found, in the online version, at https://doi.org/10.1016/j.jhydrol.2022.127657.

References

Ajami, H., Troch, P.A., Maddock, T., Meixner, T., Eastoe, C., 2011. Quantifying mountain block recharge by means of catchment-scale storage-discharge relationships. Water Resour. Res. 47 (4), W04504.
Ameli, A.A., Gabrielli, C., Morgenstern, U., McDonnell, J.J., 2018. Groundwater Subsidy From Headwaters to Their Parent Water Watershed: A Combined Field-Modeling Approach. Water Resour. Res. 54 (7), 5110–5125.
Anderson, M.P., 2008. Groundwater. Benchmark Papers in Hydrology. International Association of Hydrological Sciences, Wallingford.
Asano, Y., Kawasaki, M., Saito, T., Haraguchi, R., Takatoku, K., Saiki, M., Kimura, K., 2020. An Increase in Specific Discharge With Catchment Area Implies That Bedrock Infiltration Feeds Large Rather Than Small Mountain Headwater Streams. Water Resour. Res. 56 (9) e2019WR025658. https://agupubs.onlinelibrary.wiley.com/doi/pdf/10.1029/2019WR025658.
Asano, Y., Uchida, T., 2012. Flow path depth is the main controller of mean base flow transit times in a mountainous catchment. Water Resour. Res. 48 (3), W03512.
Bakker, M., Post, V., Langevin, C.D., Hughes, J.D., White, J.T., Starn, J.J., Fienen, M.N., 2016. Scripting MODFLOW Model Development Using Python and FloPy. Groundwater 54 (5), 733–739.
Barnhart, T.B., Molotch, N.P., Livneh, B., Harpold, A.A., Knowles, J.F., Schneider, D., 2016. Snowmelt rate dictates streamflow. Geophys. Res. Lett. 43 (15), 8006–8016.
Bear, J., 1972. Dynamics of Fluids in Porous Media. Elsevier.
Beck, H.E., van Dijk, A.I.J.M., Miralles, D.G., de Jeu (Sampurno), R.A.M., Bruijnzeel, L. A., McVicar, T.R., Schellekens, J., 2013. Global patterns in base flow index and recession based on streamflow observations from 3394 catchments. Water Resour. Res. 49 (12), 7843–7863.
Berghuijs, W.R., Hartmann, A., Woods, R.A., 2016. Streamflow sensitivity to water storage changes across Europe. Geophys. Res. Letters 43 (5), 2016GL067927.
Biswal, B., Marani, M., 2010. Geomorphological origin of recession curves. Geophys. Res. Lett. 37 (24), L24403.
Botter, G., Bertuzzo, E., Rinaldo, A., 2011. Catchment residence and travel time distributions: The master equation. Geophys. Res. Lett. 38 (11), L11403.
Brutsaert, W., 2008. Long-term groundwater storage trends estimated from streamflow records: Climatic perspective. Water Resour. Res. 44 (2), W02409.
Brutsaert, W., Nieber, J.L., 1977. Regionalized drought flow hydrographs from a mature glaciated plateau. Water Resour. Res. 13 (3), 637–643.

Burns, D.A., Murdoch, P.S., Lawrence, G.B., Michel, R.L., 1998. Effect of groundwater springs on NO3 concentrations during summer in Catskill Mountain streams. Water Resour. Res. 34 (8), 1987–1996.
Cardenas, M.B., 2007. Potential contribution of topography-driven regional groundwater flow to fractal stream chemistry: Residence time distribution analysis of Tóth flow. Geophys. Res. Lett. 34 (5), L05403.
Cardenas, M.B., Jiang, X.-W., 2010. Groundwater flow, transport, and residence times through topography-driven basins with exponentially decreasing permeability and porosity. Water Resour. Res. 46 (11), W11538.
Clark, M.P., Schaefli, B., Schymanski, S.J., Samaniego, L., Luce, C.H., Jackson, B.M., Freer, J.E., Arnold, J.R., Moore, R.D., Istanbulluoglu, E., Ceola, S., 2016. Improving the theoretical underpinnings of process-based hydrologic models. Water Resour. Res. 52 (3), 2350–2365.
Clark, M.P., Slater, A.G., Rupp, D.E., Woods, R.A., Vrugt, J.A., Gupta, H.V., Wagener, T., Hay, L.E., 2008. Framework for Understanding Structural Errors (FUSE): A modular framework to diagnose differences between hydrological models. Water Resour. Res. 44(12):W00B02.
Condon, L.E., Markovich, K.H., Kelleher, C.A., McDonnell, J.J., Ferguson, G., McIntosh, J.C., 2020. Where Is the Bottom of a Watershed? Water Resour. Res. 56 (3) e2019WR026010. https://agupubs.onlinelibrary.wiley.com/doi/pdf/10.1029/2019WR026010.
Condon, L.E., Maxwell, R.M., 2015. Evaluating the relationship between topography and groundwater using outputs from a continental-scale integrated hydrology model. Water Resour. Res. 51 (8), 6602–6621.
Dagan, G., 1989. Flow and Transport in Porous Formations. Spring-Verlag.
Dagan, G., Kroszynski, U., 1973. Drainage of a Vertical Column. In: Hadas, A., Swartzendruber, D., Rijtema, P.E., Fuchs, M., Yaron, B. (Eds.), Physical Aspects of Soil Water and Salts in Ecosystems, Ecological Studies. Springer, Berlin, Heidelberg, pp. 17–28.
Dai, X., Xie, Y., Simmons, C.T., Berg, S., Dong, Y., Yang, J., Love, A.J., Wang, C., Wu, J., 2021. Understanding topography-driven groundwater flow using fully-coupled surface-water and groundwater modeling. J. Hydrol. 594, 125950.
Dierauer, J.R., Whitfield, P.H., Allen, D.M., 2018. Climate Controls on Runoff and Low Flows in Mountain Catchments of Western North America. Water Resour. Res. 54 (10), 7495–7510.
Dingman, S.L., 2015. Physical Hydrology, third edition. Waveland Press.
Fan, Y., Clark, M., Lawrence, D.M., Swenson, S., Band, L.E., Brantley, S.L., Brooks, P.D., Dietrich, W.E., Flores, A., Grant, G., Kirchner, J.W., Mackay, D.S., McDonnell, J.J., Milly, P.C.D., Sullivan, P.L., Tague, C., Ajami, H., Chaney, N., Hartmann, A., Hazenberg, P., McNamara, J., Pelletier, J., Perket, J., Rouholahnejad-Freund, E., Wagener, T., Zeng, X., Beighley, E., Buzan, J., Huang, M., Livneh, B., Mohanty, B.P., Nijssen, B., Safeeq, M., Shen, C., Verseveld, W., Volk, J., Yamazaki, D., 2019. Hydrology in Global Change Research and Earth System Modeling. Water Resour. Res. 55 (2), 1737–1772.
Fan, Y., Li, H., Miguez-Macho, G., 2013. Global Patterns of Groundwater Table Depth. Science 339 (6122), 940–943.
Freeze, R.A., Witherspoon, P.A., 1966. Theoretical analysis of regional groundwater flow: 1. Analytical and numerical solutions to the mathematical model. Water Resour. Res. 2 (4), 641–656.
Frisbee, M.D., Phillips, F.M., Campbell, A.R., Liu, F., Sanchez, S.A., 2011. Streamflow generation in a large, alpine watershed in the southern Rocky Mountains of Colorado: Is streamflow generation simply the aggregation of hillslope runoff responses? Water Resour. Res. 47 (6), W06512.
Frisbee, M.D., Tolley, D.G., Wilson, J.L., 2017. Field estimates of groundwater circulation depths in two mountainous watersheds in the western U.S. and the effect of deep circulation on solute concentrations in streamflow. Water Resour. Res. 53 (4), 2693–2715.
Gelhar, L.W., Wilson, J.L., 1974. Ground-Water Quality Modeling. Groundwater 12 (6), 399–408.
Ghosh, D.K., Wang, D., Zhu, T., 2016. On the transition of base flow recession from early stage to late stage. Adv. Water Resour. 88, 8–13.
Gleeson, T., Befus, K.M., Jasechko, S., Luijendijk, E., Cardenas, M.B., 2016. The global volume and distribution of modern groundwater. Nat. Geosci. 9 (2), 161–167.
Gleeson, T., Manning, A.H., 2008. Regional groundwater flow in mountainous terrain: Three-dimensional simulations of topographic and hydrogeologic controls. Water Resour. Res. 44 (10), W10403.
Goderniaux, P., Davy, P., Bresciani, E., de Dreuzy, J.-R., Le Borgne, T., 2013. Partitioning a regional groundwater flow system into shallow local and deep regional flow compartments. Water Resour. Res. 49 (4), 2274–2286.
Godsey, S.E., Kirchner, J.W., 2014. Dynamic, discontinuous stream networks: hydrologically driven variations in active drainage density, flowing channels and stream order. Hydrol. Process. 28 (23), 5791–5803.
Gomez, J.D., Wilson, J.L., 2013. Age distributions and dynamically changing hydrologic systems: Exploring topography-driven flow. Water Resour. Res. 49 (3), 1503–1522.
Gomez-Velez, J.D., Krause, S., Wilson, J.L., 2014. Effect of low-permeability layers on spatial patterns of hyporheic exchange and groundwater upwelling. Water Resour. Res. 50 (6), 5196–5215.
Haitjema, H.M., Mitchell-Bruker, S., 2005. Are Water Tables a Subdued Replica of the Topography? Ground Water 43 (6), 781–786.
Harbaugh, A.W. (2005). MODFLOW-2005: the U.S. Geological Survey modular ground-water model–the ground-water flow process. U.S. Geological Survey Techniques and Methods 6–A16, U.S. Geological Survey, Reston, Virginia.
Hare, D.K., Helton, A.M., Johnson, Z.C., Lane, J.W., Briggs, M.A., 2021. Continental-scale analysis of shallow and deep groundwater contributions to streams. Nature Commun. 12 (1450).
Harman, C.J., 2015. Time-variable transit time distributions and transport: Theory and application to storage-dependent transport of chloride in a watershed. Water Resour. Res. 51 (1), 1–30.
Harman, C.J., Sivapalan, M., Kumar, P., 2009. Power law catchment-scale recessions arising from heterogeneous linear small-scale dynamics. Water Resour. Res. 45 (9), W09404.
Huang, X., Niemann, J.D., 2006. Modelling the potential impacts of groundwater hydrology on long-term drainage basin evolution. Earth Surf. Proc. Land. 31 (14), 1802–1823.
Ingebritsen, S.E., Manning, C.E., 1999. Geological implications of a permeability-depth curve for the continental crust. Geology 27 (12), 1107–1110.
Iwasaki, K., Nagasaka, Y., Nagasaka, A., 2021. Geological Effects on the Scaling Relationships of Groundwater Contributions in Forested Watersheds. Water Resour. Res. 57 (7) e2021WR029641. eprint: https://agupubs.onlinelibrary.wiley.com/doi/pdf/10.1029/2021WR029641.
Jasechko, S., Kirchner, J.W., Welker, J.M., McDonnell, J.J., 2016. Substantial proportion of global streamflow less than three months old. Nat. Geosci. 9 (2), 126–129.
Jiang, X.-W., Wan, L., Wang, J.-Z., Yin, B.-X., Fu, W.-X., Lin, C.-H., 2014. Field identification of groundwater flow systems and hydraulic traps in drainage basins using a geophysical method. Geophys. Res. Letters 41 (8), 2014GL059579.
Kaushal, S.S., Likens, G.E., Pace, M.L., Utz, R.M., Haq, S., Gorman, J., Grese, M., 2018. Freshwater salinization syndrome on a continental scale. Proc. Nat. Acad. Sci. 115 (4), E574–E583.
Kazemi, G.A., Lehr, J.H., Perrochet, P., 2006. Groundwater Age. John Wiley & Sons.
Kirchner, J.W., 2009. Catchments as simple dynamical systems: Catchment characterization, rainfall-runoff modeling, and doing hydrology backward. Water Resour. Res. 45 (2), W02429.
Krakauer, N.Y., Li, H., Fan, Y., 2014. Groundwater flow across spatial scales: importance for climate modeling. Environ. Res. Lett. 9 (3), 034003.
Lovill, S.M., Hahm, W.J., Dietrich, W., 2018. Drainage from the Critical Zone: Lithologic Controls on the Persistence and Spatial Extent of Wetted Channels during the Summer Dry Season. Water Resour. Res. 54 (8), 5702–5726.
Luo, Y., Arnold, J., Allen, P., Chen, X., 2012. Baseflow simulation using SWAT model in an inland river basin in Tianshan Mountains, Northwest China. Hydrol. Earth Syst. Sci. 16 (4), 1259–1267.
Lyon, S.W., Koutsouris, A., Scheibler, F., Jarsjö, J., Mbanguka, R., Tumbo, M., Robert, K. K., Sharma, A.N., Velde, Y.V.D., 2015. Interpreting characteristic drainage timescale variability across Kilombero Valley, Tanzania. Hydrol. Processes 29 (8), 1912–1924.
Maher, K., Chamberlain, C.P., 2014. Hydrologic Regulation of Chemical Weathering and the Geologic Carbon Cycle. Science 343 (6178), 1502–1504.
Manning, A.H., 2011. Mountain-block recharge, present and past, in the eastern Espanola Basin, New Mexico, USA. Hydrogeology Journal 19 (2), 379–397.
Manning, A.H., Solomon, D.K., 2005. An integrated environmental tracer approach to characterizing groundwater circulation in a mountain block. Water Resour. Res. 41 (12).
McDonnell, J.J., Beven, K., 2014. Debates—The future of hydrological sciences: A (common) path forward? A call to action aimed at understanding velocities, celerities and residence time distributions of the headwater hydrograph. Water Resour. Res. 50 (6), 5342–5350.
McGuire, K.J., McDonnell, J.J., Weiler, M., Kendall, C., McGlynn, B.L., Welker, J.M., Seibert, J., 2005. The role of topography on catchment-scale water residence time. Water Resour. Res. 41 (5), W05002.
Miller, M.P., Buto, S.G., Susong, D.D., Rumsey, C.A., 2016. The importance of base flow in sustaining surface water flow in the Upper Colorado River Basin. Water Resour. Res. 52 (5), 3547–3562.
Mutzner, R., Bertuzzo, E., Tarolli, P., Weijs, S.V., Nicotina, L., Ceola, S., Tomasic, N., Rodriguez-Iturbe, I., Parlange, M.B., Rinaldo, A., 2013. Geomorphic signatures on Brutsaert base flow recession analysis. Water Resour. Res. 49 (9), 5462–5472.
Niswonger, R.G., Panday, S., and Ibaraki, M. (2011). MODFLOW-NWT, A Newton Formulation for MODFLOW-2005. U.S. Geological Survey Techniques and Methods 6–A37, U.S. Geological Survey, Reston, VA.
Pauritsch, M., Birk, S., Wagner, T., Hergarten, S., Winkler, G., 2015. Analytical approximations of discharge recessions for steeply sloping aquifers in alpine catchments. Water Resour. Res. 51 (11), 8729–8740.
Peralta-Tapia, A., Sponseller, R.A., Ågren, A., Tetzlaff, D., Soulsby, C., Laudon, H., 2015. Scale-dependent groundwater contributions influence patterns of winter baseflow stream chemistry in boreal catchments. J. Geophys. Res. Biogeosci. 120 (5), 2014JG002878.
Perron, J.T., Kirchner, J.W., Dietrich, W.E., 2008. Spectral signatures of characteristic spatial scales and nonfractal structure in landscapes. J. Geophys. Res.: Earth Surface 113 (F4), F04003.
Piovano, T., Tetzlaff, D., Maneta, M., Buttle, J.M., Carey, S.K., Laudon, H., McNamara, J., Soulsby, C., 2020. Contrasting storage-flux-age interactions revealed by catchment inter-comparison using a tracer-aided runoff model. J. Hydrol. 590, 125226.
Pollock, D.W. (2012). User Guide for MODPATH Version 6–A Particle-Tracking Model for MODFLOW. U.S. Geological Survey Techniques and Methods 6–A41, U.S. Geological Survey, Reston, Virginia.
Prancevic, J.P., Kirchner, J.W., 2019. Topographic Controls on the Extension and Retraction of Flowing Streams. Geophys. Res. Lett. 46 (4), 2084–2092.
Rademacher, L.K., Clark, J.F., Clow, D.W., Hudson, G.B., 2005. Old groundwater influence on stream hydrochemistry and catchment response times in a small Sierra Nevada catchment: Sagehen Creek, California. Water Resour. Res. 41 (2).
Rapp, G.A., Condon, L.E., Markovich, K.H., 2020. Sensitivity of Simulated Mountain Block Hydrology to Subsurface Conceptualization. Water Resour. Res. 56 (10) e2020WR027714. eprint: https://onlinelibrary.wiley.com/doi/pdf/10.1029/2020WR027714.

Rodríguez-Iturbe, I., Rinaldo, A., 1997. Fractal River Basins: Chance and Self-Organization. Cambridge University Press.
Rumsey, C.A., Miller, M.P., Susong, D.D., Tillman, F.D., Anning, D.W., 2015. Regional scale estimates of baseflow and factors influencing baseflow in the Upper Colorado River Basin. J. Hydrol.: Regional Studies 4 (Part B), 91–107.
Rupp, D.E., Selker, J.S., 2006. On the use of the Boussinesq equation for interpreting recession hydrographs from sloping aquifers. Water Resour. Res. 42 (12).
Sabo, R.D., Nelson, D.M., Eshleman, K.N., 2016. Episodic, seasonal, and annual export of atmospheric and microbial nitrate from a temperate forest. Geophys. Res. Lett. 43 (2), 683–691.
Santhi, C., Allen, P.M., Muttiah, R.S., Arnold, J.G., Tuppad, P., 2008. Regional estimation of base flow for the conterminous United States by hydrologic landscape regions. J. Hydrol. 351 (1–2), 139–153.
Smerdon, B.D., Payton Gardner, W., Harrington, G.A., Tickell, S.J., 2012. Identifying the contribution of regional groundwater to the baseflow of a tropical river (Daly River, Australia). J. Hydrol. 464, 107–115.
Stephens, D.B., Umstot, T., 2019. Development and evaluation of the Maxey-Eakin recharge method. Hydrogeol. J. 27 (2), 747–760.
Stoddard, J.L., 1994. Long-Term Changes in Watershed Retention of Nitrogen. In: Environmental Chemistry of Lakes and Reservoirs, volume 237 of Advances in Chemistry. American Chemical Society, pp. 223–284.
Stoelzle, M., Stahl, K., Morhard, A., Weiler, M., 2014. Streamflow sensitivity to drought scenarios in catchments with different geology. Geophys. Res. Lett. 41 (17), 2014GL061344.
Stoelzle, M., Weiler, M., Stahl, K., Morhard, A., Schuetz, T., 2015. Is there a superior conceptual groundwater model structure for baseflow simulation? Hydrol. Process. 29 (6), 1301–1313.
Tague, C., Grant, G.E., 2004. A geological framework for interpreting the low-flow regimes of Cascade streams, Willamette River Basin. Oregon. Water Resour. Res. 40 (4).
Tartakovsky, G.D., Neuman, S.P., 2007. Three-dimensional saturated-unsaturated flow with axial symmetry to a partially penetrating well in a compressible unconfined aquifer. Water Resour. Res. 43, W01410.
Teuling, A.J., Lehner, I., Kirchner, J.W., Seneviratne, S.I., 2010. Catchments as simple dynamical systems: Experience from a Swiss prealpine catchment. Water Resour. Res. 46 (10), W10502.
Tomer, M.D., Burkart, M.R., 2003. Long-term effects of nitrogen fertilizer use on ground water nitrate in two small watersheds. J. Environ. Qual. 32 (6), 2158–2171.
Tóth, J., 1963. A theoretical analysis of groundwater flow in small drainage basins. J. Geophys. Res. 68 (16), 4795–4812.
Tóth, J., 2009. Gravitational Systems of Groundwater Flow: Theory, Evaluation, Utilization. Cambridge University Press, New York, USA.
Trancoso, R., Larsen, J.R., McVicar, T.R., Phinn, S.R., McAlpine, C.A., 2017. CO2-vegetation feedbacks and other climate changes implicated in reducing base flow. Geophys. Res. Lett. 44 (5), 2310–2318.
Troch, P.A., Berne, A., Bogaart, P., Harman, C., Hilberts, A.G.J., Lyon, S.W., Paniconi, C., Pauwels, V.R.N., Rupp, D.E., Selker, J.S., Teuling, A.J., Uijlenhoet, R., Verhoest, N.E. C., 2013. The importance of hydraulic groundwater theory in catchment hydrology: The legacy of Wilfried Brutsaert and Jean-Yves Parlange. Water Resour. Res. 49 (9), 5099–5116.
Valett, H.M., Morrice, J.A., Dahm, C.N., Campana, M.E., 1996. Parent lithology, surface–groundwater exchange, and nitrate retention in headwater streams. Limnol. Oceanogr. 41 (2), 333–345.
van der Velde, Y., Torfs, P.J.J.F., van der Zee, S.E.A.T.M., Uijlenhoet, R., 2012. Quantifying catchment-scale mixing and its effect on time-varying travel time distributions. Water Resour. Res. 48 (6), W06536.
Wang, C., Gomez-Velez, J.D., Wilson, J.L., 2018. The Importance of Capturing Topographic Features for Modeling Groundwater Flow and Transport in Mountainous Watersheds. Water Resour. Res. 54 (12), 10,313–10,338.
Welch, L.A., Allen, D.M., 2014. Hydraulic conductivity characteristics in mountains and implications for conceptualizing bedrock groundwater flow. Hydrogeol. J. 22 (5), 1003–1026.
Wilson, J.L., Guan, H., 2004. Mountain-Block Hydrology and Mountain-Front Recharge. In: Hogan, J.F., Phillips, F.M., Scanlon, B.R. (Eds.), Groundwater Recharge in a Desert Environment: The Southwestern United States. American Geophysical Union, pp. 113–137.
Winter, T.C., Harvey, J.W., Franke, O.L., and Alley, W.M. (1998). Ground Water and Surface Water A Single Resource. U.S. Geological Survey Circular 1139, U.S. Geological Survey, Denver, Colorado.
Wörman, A., Packman, A.I., Marklund, L., Harvey, J.W., Stone, S.H., 2006. Exact three-dimensional spectral solution to surface-groundwater interactions with arbitrary surface topography. Geophys. Res. Lett. 33 (7), L07402.
Wörman, A., Packman, A.I., Marklund, L., Harvey, J.W., Stone, S.H., 2007. Fractal topography and subsurface water flows from fluvial bedforms to the continental shield. Geophys. Res. Lett. 34 (7).
Yadav, M., Wagener, T., Gupta, H., 2007. Regionalization of constraints on expected watershed response behavior for improved predictions in ungauged basins. Adv. Water Resour. 30 (8), 1756–1774.
Yao, Y., Zheng, C., Andrews, C., Zheng, Y., Zhang, A., Liu, J., 2017. What controls the partitioning between baseflow and mountain block recharge in the Qinghai-Tibet Plateau? Geophys. Res. Lett. 44 (16), 8352–8358.
Zecharias, Y.B., Brutsaert, W., 1988. The influence of basin morphology on groundwater outflow. Water Resour. Res. 24 (10), 1645–1650.
Zecharias, Y.B., Brutsaert, W., 1988. Recession characteristics of groundwater outflow and base flow from mountainous watersheds. Water Resour. Res. 24 (10), 1651–1658.
Zhang, Y., Person, M., Voller, V., Cohen, D., McIntosh, J., Grapenthin, R., 2018. Hydromechanical Impacts of Pleistocene Glaciations on Pore Fluid Pressure Evolution, Rock Failure, and Brine Migration Within Sedimentary Basins and the Crystalline Basement. Water Resour. Res. 54 (10), 7577–7602 eprint: https://agupubs.onlinelibrary.wiley.com/doi/pdf/10.1029/2017WR022464.
Zlotnik, V.A., Cardenas, M.B., Toundykov, D., 2011. Effects of Multiscale Anisotropy on Basin and Hyporheic Groundwater Flow. Ground Water 49 (4), 576–583.